Morphology-based characterization of intermediate to silicic lava flows: Application to the Central Andean Volcanic Zone

Jose Pablo Sepulveda, Raffaello Cioni, Alvaro Aravena

Earth-Science Reviews 241 (2023) 104433

Contents lists available at ScienceDirect

Earth-Science Reviews

journal homepage: www.elsevier.com/locate/earscirev

Morphology-based characterization of intermediate to silicic lava flows: Application to the Central Andean Volcanic Zone

Jose Pablo Sepulveda [a,b,*], Raffaello Cioni [a], Alvaro Aravena [c,d]

[a] Dipartimento di Scienze della Terra, Università degli studi di Firenze, Via Giorgio la Pira, 4, 50121 Florence, Italy
[b] Millennium Institute on Volcanic Risk Research - Ckelar Volcanoes, Avenida Angamos, 0610, Antofagasta, Chile
[c] Laboratoire Magmas et Volcans, Université Clermont Auvergne, CNRS, IRD, OPGC, 6 Avenue Blaise Pascal, Aubière, France
[d] Facultad de Ciencias Básicas, Universidad Católica del Maule, Avenida San Miguel 3605, Talca, Chile

ARTICLE INFO

Keywords:
Lava flow morphology
Dacite
Andes
Blocky lava
Folds

ABSTRACT

The morphology of a lava flow records the eruptive dynamics that governed its emplacement, evolution, and the rheological properties of the erupted magma. Although the dynamics and morphological classification of mafic lava flows have been widely addressed, the characterization of the morphological features of intermediate to silicic lavas is still not exhaustive. In this study, we perform a morphological-based characterization of lava flows based on DEM-derived data and satellite images. We analyzed a dataset of 49 intermediate to silicic lava flows from the Central Andean Volcanic Zone and quantified the maximum wavelength of their surface ridges, described as folds, and their relationship with thickness distribution, pre-surface slope, composition, and rheology. Furthermore, we introduced a Fourier analysis to quantitatively characterize the lava flows' plain-view shape and a novel method based on an S-Transform spectral analysis of grayscale satellite images to assess the surface folding pattern. We distinguish 4 main types of lava flows in the andesite to dacite compositional range. *Ridged lavas* have highly arcuate ridges with convex surfaces, large thickness, and a curved, smooth frontal lobe. *Coulee lavas* have intermediate characteristics between lava flows and domes, with relatively simple shapes, lengths that do not significantly exceed their width, vents generally located in the central zone of the flow, prominent ridges and crumble breccias. *Leveed lavas*, which include a wide range of flow lengths, have the simplest shapes, exhibiting marked channelization and a unique frontal toe of maximum thickness. *Breakout lavas* have the most complex plain-view shapes, with lateral and frontal lobes, poorly developed levees, and wider and thicker fronts. *Transitional lavas,* with intermediate characteristics in terms of folding patterns and shapes, are also recognized. We show that the maximum wavelength of surface deformation is not continuous along the flow surface and spatially correlates with thickness distribution. In addition, the maximum wavelength is poorly correlated with SiO_2 content and weakly correlated with lava viscosity, showing a positive correlation with the gravitational component of the shear stress applied to the flow. Results suggest that the pre-eruptive slope and viscosity, along with the effusion rate, play a primary role in governing the general dynamics of the flow and thus the resulting lava morphology, impacting different measurable features such as length, width, branching, and general deformation dynamics of the flow. The recognition of the main characteristics of the different lava types and their controlling factors represents a first step for interpreting lava flow morphology in terms of the eruption characteristics. This strategy can be adopted to analyze and interpret terrestrial and extra-terrestrial lava flows remotely.

1. Introduction

Lava flows are the most common eruptive products on Earth and extra-terrestrial surfaces. They exhibit a wide variation spectrum in terms of composition, size, shape, and surface and internal structures, varying from thin flows with relatively smooth surfaces to voluminous lava flows hundreds of meters thick (Kilburn, 2000; Harris and Rowland, 2015). The morphological characteristics of lava flows are a consequence of the combined effect of eruption source parameters (e.g., effusion rate and source geometry), magma properties (e.g., rheology,

* Corresponding author at: Dipartimento di Scienze della Terra, Università degli studi di Firenze, Via Giorgio la Pira, 4, 50121 Florence, Italy.
E-mail address: josepablo.sepulvedabirke@unifi.it (J.P. Sepulveda).

https://doi.org/10.1016/j.earscirev.2023.104433
Received 30 December 2021; Received in revised form 4 April 2023; Accepted 17 April 2023
Available online 24 April 2023

controlled by composition, temperature, and crystal content), and the characteristics of the terrain over which the lavas flowed (Hulme, 1974; Griffiths et al., 2003; Lescinsky et al., 2007). Thus, the morphology of a given lava flow can provide insights into the erupted magma properties and emplacement processes (Griffiths and Fink, 1992a, 1992b; Chevrel et al., 2013; Tolometti et al., 2020), allowing us to understand the fundamental parameters and dynamics that controlled the eruption.

In order to characterize and classify the lava flows, a frequently adopted strategy is based on a descriptive tripartite classification related to their surfaces or the presence of peculiar features, including pahoehoe, a'ā, and blocky lavas (Jones, 1943; Macdonald, 1953). Several studies have focused on active pahoehoe and a'ā lava flows (e.g., at Hawaii, Mt. Etna, Iceland, among other case studies) and on analog laboratory experiments to simulate basaltic flows (Hallworth et al., 1987; Fink and Griffiths, 1990; Griffiths and Fink, 1992a, 1992b; Gregg and Fink, 1995, 1996, 2000; Kerr et al., 2006). Thanks to them, the emplacement dynamics of mafic flows are reasonably well-understood, and a robust morphological classification has been developed. Subgroups are mainly derived from a complete intergradation between pahoehoe and a'ā lavas, with particular characteristics typically belonging to both groups (Jones, 1943; Macdonald, 1953; Wentworth and Macdonald, 1953; Macdonald, 1967; Fink and Fletcher, 1978; Kilburn, 1990; Harris et al., 2016, and references therein). However, these subtypes are generally defined qualitatively and are typically based on the morphology of the flow interiors, including the presence, size, shape, and distribution of vesicles, as well as the presence and type of shear structures (Harris et al., 2016), being univocal and in some cases subjective.

Regarding highly evolved lavas, increasing attention has been paid during the last decades (Fink, 1980, 1983; De Silva et al., 1994; Castro and Cashman, 1999; Castro et al., 2002; Harris et al., 2002; Pyle and Elliott, 2006; Lescinsky et al., 2007; Tuffen et al., 2013; Castro et al., 2013; Farquharson et al., 2015; Magnall et al., 2017, 2018; Bullock et al., 2018; Deardorff et al., 2019; Leggett et al., 2020; Andrews et al., 2020). Most of these studies have been focused on rhyolitic and/or obsidian-like flows, while, even though a suite of investigations on specific case studies is available in the literature (Borgia and Linneman, 1990; Naranjo et al., 1992; De Silva et al., 1994; Watts et al., 2002; Harris et al., 2002; Cioni and Funedda, 2005; Pyle and Elliott, 2006; Vallance et al., 2008; Latutrie et al., 2017; among others), less attention has been paid to the analysis of the general laws controlling the evolution and emplacement of lavas in the andesite-to-dacite compositional range.

In this study, we present a morphology-based characterization of andesitic to dacitic lavas based on the analysis of easily accessed satellite imagery and topographic data, considering their plain-view shape, thickness and characteristics of the upper surface. In particular, we analyze the surface texture in terms of folding patterns and maximum wavelength, and we also evaluate their relationship with thickness distribution, pre-surface slope, composition, and rheology. In addition, we introduce a Fourier Descriptors analysis for quantifying the plain-view shape of the lava flows and a novel method based on a S-transform spectral analysis of grayscale satellite image data to describe the surface folding pattern quantitatively. On the basis of our remote characterization, we define 4 main categories for intermediate to silicic lava flows. We conclude that the investigated lava flows cannot be distinguished only based on few simple, univocal characteristics (like for example the pahoehoe or a'ā surface of basaltic lavas) but by a sum of multiple observations. Although this fact does not allow to build a real "classification scheme" (where classification is intended as "a systematic arrangement in groups or categories according to established criteria; Dictionary and Merrian-Webster, 2002" and in which each group is strictly defined by a list of univocal criteria), the recognition and systematic characterization of some morphological features can inform about the main processes controlling the emplacement and final morphology of these lava flows.

2. Background on lava flow morphology-based classification

2.1. Blocky lavas and folding

In the study of intermediate to silica-rich lavas, which are frequently characterized by the accumulation of angular blocks formed by the breakage of the rigid upper lava surface, a commonly adopted descriptive term is blocky-lava (Finch, 1933). This general term was introduced to describe flows composed of blocks that may not fill with pahoehoe and a'ā lavas and is used for both obsidian-like and crystal-rich flows, with variable features of banding, shear patterns, foliation, folding, and eventual blocky and/or rubbly breccias (Macdonald, 1972; Fink, 1980; Cas and Wright, 1988; Kilburn, 1990, 2000; Anderson and Fink, 1992; Cioni and Funedda, 2005; Harris et al., 2016; Leggett et al., 2020). However, obsidian-like and crystal-rich flows present different rheological and morphological features, and a wide variety of deformation patterns are expected to operate during their emplacement (Table 1).

Silica-rich, obsidian-like flows are characterized by autobrecciated upper surfaces and by a complex internal sequence that typically includes four lithofacies: lithoidal rhyolite (i.e., welded, generally devitrified), coarsely vesicular pumice, flow-banded obsidian, and fine vesicular pumice (Fink, 1983; Manley and Fink, 1987; Castro and Cashman, 1999, Bullock et al., 2018, Table 1). Multiple generations and scales of ogives and crease structures occur along with the upper surface of the flow. Although these ogives were first interpreted as derived from the folding of the upper portion of the lava flow (Fink, 1980), other authors suggest they suggested that they are fracture-bound structures rather than folds (Cas and Wright, 1988; Andrews et al., 2020). While obsidian lava flows remain the most studied examples of silicic flows, Cioni and Funedda (2005) showed how deformation of crystal-rich,

Table 1
Summary of the main characteristics for obsidian-like flows and crystalline andesites to dacites. FVP: fine vesicular pumice, CVP: coarse vesicular pumice. [a] Fink (1983), [b] Manley and Fink (1987), [c] Bullock et al. (2018), [d] Andrews et al. (2020), [e] Harris et al. (2016), [f] Cioni and Funedda (2005), [g] Cas and Wright (1988).

Lava type	Stratigraphy	Structures	Deformation mechanism
Obsidian like Rhyolitic	(i) basal breccia, (ii) thin layered obsidian with spherulites, (iii) devitrified to crystalline rhyolite, (iv) thick obsidian ranging from FVP lithofacies with small irregular-to-acicular vesicles to alternating centimeter-scale layers of obsidian with centimeter to meter-scale layers of CVP lithofacies, and (v) upper breccia [a, b, c]	Ogive Crease Autobreccia	Mainly brittle, disrupting and tilting of the surface [d, e]
Crystal rich andesites to dacites (rhyolites)	Basal auto-breccia with a massive core, sometimes well-developed flow foliation, columnar or blocky jointing, and a top breccia ranging from large subrounded rubbly clast to sub-angular obsidian and lithoid blocks [e, f, g]	Ridge Folds Ramps Crease Foliation Autobreccia	Synemplacement progressive folding due to compression. Thrust and ramp structures in the frontal sectors. [f]

lithoid silicic lava flows could develop different structures compared to glassy lavas, with the formation of foliation surfaces that mainly control the lava movement. Formation of different fold generations was clearly demonstrated in these lava flows (e.g. Figs. 8 and 9 in Cioni and Funedda, 2005; Harris and Rowland, 2015), while nearly vertical fracture planes (ramps) mainly develop in the frontal sectors of the lava flows where maximum strain accumulated. Similarly, andesites and dacites are often pervasively foliated and fractured, with basal and top breccias. Ridges occur on the flow surface as alternating arcuate peaks and troughs with the concavity arranged perpendicular to the flow direction in the central portions of the channel and subparallel to the flow direction along the outer margins (Fink, 1980; Cioni and Funedda, 2005).

By analogy with crystal-rich silicic lava flows, we interpret the ridge structures in andesites and dacites as folds formed by compression. The relatively rigid, rapidly solidified crust deforms with a brittle behavior forming the upper blocky surface, while the rest of the lava body deforms plastically, inducing shear (Cioni and Funedda, 2005; Pyle and Elliott, 2006; Lescinsky et al., 2007; Deardorff et al., 2019). At the base of these lavas, superimposed penetrative foliations may govern folding (Cioni and Funedda, 2005). Shear planes associated with these foliations are flow-parallel at the margins of the lava and sub-horizontal to the flow base (Cioni and Funedda, 2005) and may act as sliding surfaces triggering folding at different scales of the entire inner flow and surface ridges or as ramp structures, arranging the movement and deformation of the flow through faulting during stick-slip processes (Cas and Wright, 1988; Cioni and Funedda, 2005; Harris et al., 2016). Superimposed generations of folds with progressively increasing wavelength and amplitude form when the tightly-arranged, first-generation folds can no longer accommodate further flow-parallel shortening, and compressional forces continue to act on the flow. The blocky surface of these lavas may be rapidly removed by erosion, leaving uncovered the internal, deformed part of the flow (Fink, 1980; Gregg et al., 1998; Cioni and Funedda, 2005; Farrell et al., 2018). Brittle deformation dominates at the front of the lava flow or during the final phases of its emplacement, forming crease structures and tensile fractures (Anderson and Fink, 1992; Cioni and Funedda, 2005).

2.2. Lava flow morphology from analog experiments

Analog experiments on lava flow morphology may help to classify the shape and morphological features of silicic lava flows, although many of these experiments were planned to simulate basaltic lavas. Hallworth et al. (1987)investigated the role of effusion rate, slope, and viscosity-temperature dependence in determining the morphology of basaltic lava flows. They qualitatively classified lava flows into (1) straight, open-channel flows, with a single flow and a straight open channel bounded by levees; (2) meandering, temporarily roofed flows with overflow and breakout at their margins, and (3) compound flows, characterized by the establishment of tube systems. Later, Fink and Griffiths (1990) investigated the effect of a solidifying crust on the dynamics and surface morphology of radial viscous-gravity currents. They experimented with PEG wax, producing five distinct flow morphologies by systematically varying the cooling and effusion rates: pillows, rift, folded, levees, and no-crust flows. Griffiths and Fink (1992a) proposed that the ratio between the characteristic times of surface solidification and lateral flow advection is strictly related to the surface morphology. Many other studies from the same group furtherly refined these observations (Griffiths, 2000 and references therein).

The attempts to classify morphologically more evolved, high-viscosity lavas mainly focused on domes. Blake (1990) defined four types of domes: upheaved plugs, peleean, low lava, and coulees. Afterward, Griffiths and Fink (1997) and Fink and Griffiths (1998) combined experimental models with field measurements of active extrusions and remote sensing observation of Holocene domes. They showed that the morphology of lava domes is related to their eruption conditions and classified them into four main types; spiny, lobate, platy, and axisymmetric domes. They also suggested that eruption conditions could be related through a dimensionless parameter encompassing the eruption rate, magma rheology, and thickness of the cooling surface. Finally, Lyman et al. (2004) performed laboratory experiments with a PEG-kaolin slurry extruded into cold water, testing variable experimental conditions in the slope, effusion rate, and water temperature. They distinguished four types of domes and related lava flows morphologies: (1) spiny domes, with spine-like lobes similar to an up-heaved plug; (2) lobate flows, characterized by smooth sides and wave-like ridges; (3) platy flows, with a rough surface with small step-like ridges, and (4) no-crust flows, which typically develop a crust only in their outermost margins. Transitions between the different morphologies commonly occur. In addition, they calculated the yield strength or effusion rate for lava domes based on their morphology, slope and ψ_B, suggesting the following equation:

$$\psi_B = (g\Delta\rho/\sigma_0)^3 Qt_s \quad (1)$$

where g is gravitational acceleration, Δ_Q is the density difference between magma and the environment, σ_0 is the yield strength, Q is the volumetric effusion rate and t_s is the characteristic time for surface solidification.

3. Methods

The observation of structures on the scale of meters to hundreds of meters in andesitic to dacitic lava flows clearly shows that a set of surface features may be introduced to complement the classification schemes summarized above, particularly for leeved or folded flows. For this reason, we present in this section a series of procedures to characterize quantitatively the surface structures and morphology of a wide set of intermediate to silicic lava flows.

3.1. The lava flow dataset

We selected a large set of examples from the Andes Central Volcanic Zone (CVZ) to address the morphological characteristics of intermediate lava flows. The CVZ was selected due to the relatively restricted compositional range that characterizes this volcanic arc (mainly andesitic to dacitic magmas; Stern, 2004; Wörner et al., 2018). The hyper-arid climate conditions since the Miocene (Dunai et al., 2005) caused the formation of unvegetated surfaces and extremely-low erosion rates, so that a remarkable number of stratovolcanoes and lava flows with well-preserved surface structures are present. This study includes 49 andesitic to dacitic lava flows emplaced during the Pleistocene (Table 2, Supplementary material 1) selected from 27 volcanic systems, with compositions ranging from 58.7 to 68.3 wt% SiO_2. These lava flows account for a wide spectrum of morphological features, with well-preserved ridges, creases, levees, and crumble breccia structures.

3.2. Compiled information and lava flow characterization

3.2.1. Analysis of DEM-derived data

We adopted a 12 m TanDEM-X (Krieger et al., 2007) for most of the studied lava flows and an ALOS PALSAR DEM (12.5 m pixel resolution) for Tata Sabaya, Isluga, El Misti, and Uturuncu volcanoes. Topographic data were used to extrapolate the pre-eruptive surface, thickness, volume, and roughness for each lava flow.

Following Kereszturi et al. (2016), the pre-eruptive topography covered by a given lava flow was approximated to a planar surface. It was created from a set of a digitalized rectangular mesh of points, spaced 2 m apart from each other, along the margins of the lava flow unit. Height values were extracted from the DEM and assigned to each point, while all points located within the lava flow boundary were subtracted from the mesh. Then, the pre-eruptive surface was modeled by adopting

Table 2
Dataset of the studied CVZ lava flows. * = not analyzed, – = not available data, Λ = Maximum wavelength / second maximum wavelength, $P_{k>95}$ = value of k at which $P(k)$ exceeds 0.95. Cxs = crystallinity; only includes phenocrysts, while thickness, runout, and width referrers to maximum values. Yield strength is calculated as a function of thickness, density (2500 kgm^{-3}), the gravity acceleration constant (9.81 ms^{-2}) and the slope, while effusion rates were obtained following eq. 12 (see section 5.5). Volcanoes with more than one flow include an abbreviation to differentiate them. N = north, S = south, E = east, NW = northwest, SW = southwest, W = west, E1 = East 1, = E2 = East 2, M = middle, L = lower, U = upper.

Flow	Type (this work)	Maximum wavelength (m)	Second maximum wavelength (m)	Λ	Thickness (m)	Runout (km)	Width (m)	Pre-eruptive slope (°)	SiO_2 (%wt)	Cxs (wt %)	Pk > (95)	Vol (km^3)	Yield strenght (Mpa)	Effusion rate (m^3s^{-1})	Area (km^2)	Reference
Acotango	Ridged	141	84	1.68	236	6.17	2292	16.66	–	–	6	0.778	632	203.41	8.66	–
Cerro Bayo N	Ridged	228	142	1.61	173	3.45	1571	20.98	–	–	5	0.344	598	139.17	5.05	–
Cerro Bayo S	Ridged	244	169	1.44	210	3.86	1582	28.07	66.53	–	4	0.32	993	178.53	3.72	Naranjo et al. (2013)
Chao dacite	Ridged	274	244	1.12	344	14.27	7239	11.65	68.28	48	7	9.25	768	170.17	59.61	De Silva et al. (1994)
Ollagüe NW	Ridged	90	71	1.27	132	3.29	1183	32.75	63.26	–	3	0.133	712	130.04	2.48	Mamani et al. (2010)
Acamarachi	Coulee	120	84	1.43	103	2.95	2306	13.3	–	–	7	0.217	167	0.48	7.35	–
Colachi	Coulee	94	53	1.77	85	1.77	1396	20.74	–	–	5	0.064	253	1.68	2.2	–
Chac-Inca W	Coulee	106	96	1.10	180	2.85	2596	15.68	67.04	45	5	0.549	577	20.00	6.31	Selles and Gardeweg (2018)
Chac-Inca E	Coulee	93	70	1.33	144	1.30	1310	18.25	–	45	2	0.123	468	1.07	2.02	Selles and Gardeweg (2018)
Ollagüe N	Coulee	*	*	*	196	2.00	1608	20.48	64.49	30	2	0.165	659	11.91	2.15	Feeley et al. (1993)
Lllullaillaco N	Leveed	146	102	1.43	164	5.32	3475	30.57	65.83	17	*	0.27	720	29.78	4.68	Gardeweg et al. (1984)
Olca Paruma M	Leveed	88	65	1.35	81	2.44	847	14.1	63.06	33	5	0.046	210	206.54	1.31	Martinez (2019)
Tata Sabaya NW	Leveed	215	142	1.51	125	3.82	886	31.68	–	–	4	0.145	759	19.92	2.46	–
Tata Sabaya SW	Leveed	97	56	1.73	120	3.51	853	34.84	61.11	–	4	0.082	580	221.87	1.98	De Silva et al. (1993)
Sairecabur N	Leveed	85	50	1.70	54	1.59	633	14.91	61.2	–	7	0.012	118	77.04	0.64	Mamani et al. (2010)
Putana SW	Leveed	78	35	2.23	70	1.80	813	26.88	–	–	4	0.023	266	3.34	0.96	–
Falso Azufre M	Leveed	66	44	1.50	122	4.04	995	16.62	–	–	5	0.086	220	14.01	2.74	–
Irruputuncu L	Leveed	153	110	1.39	100	2.72	958	27.77	59.72	27	2	0.057	306	18.62	2.13	Rodriguez et al. (2015)
Irruputuncu U	Leveed	70	44	1.59	167	1.51	865	36.67	62.4	27	2	0.064	987	19.87	0.95	Wörner et al. (1992)
Llullaillaco U	Leveed	70	41	1.71	152	3.33	928	43.88	65.42	30	2	0.098	712	327.97	2.34	Gardeweg et al. (1984)
Putana S	Leveed	58	45	1.29	77	1.03	690	32.9	–	–	3	0.014	339	70.59	0.55	–
Condor	Leveed	118	82	1.44	92	4.67	799	22.22	65.2	–	5	0.056	213	17.93	2.44	Grosse et al. (2018)
Socompa S	Leveed	*	*	*	210	5.11	1643	16.52	–	–	5	0.488	516	10.56	6.59	–
Lascar N	Leveed	98	60	1.63	93	4.15	836	25.03	63.97	–	6	0.083	388	242.34	2.22	Gardeweg et al. (2011)
Socompa SW	Leveed	*	*	*	106	3.99	1021	30.02		–	5	0.105	420	50.73	3.07	–
San Pedro N	Breakout	285	257	1.11	139	5.65	1533	14.35	64	8	13	0.271	299	42.82	5.51	Bertin and Amigo (2019)
San Pedro NW	Breakout	220	137	1.61	151	5.96	2415	9.78	65.5	10	14	0.51	269	7.98	7.89	Bertin and Amigo (2019)
Isluga	Breakout	120	66	1.82	72	3.01	1117	11.67	58.72	28	14	0.036	88	0.25	2.04	Cascante (2015)
Guallatiri	Breakout	98	60	1.63	182	2.33	937	13.82	63.4	35	8	0.124	472	35.65	1.54	Sepulveda et al. (2021)

(*continued on next page*)

Table 2 (*continued*)

Flow	Type (this work)	Maximum wavelength (m)	Second maximum wavelength (m)	Λ	Thickness (m)	Runout (km)	Width (m)	Pre-eruptive slope (°)	SiO_2 (%wt)	Cxs (wt %)	Pk > (95)	Vol (km^3)	Yield strenght (Mpa)	Effusion rate (m^3s^{-1})	Area (km^2)	Reference
Licancabur N	Breakout	74	53	1.40	59	2.81	726	16.72	60.5	< 12	14	0.036	181	1.78	1.4	Figueroa et al. (2009)Mamani et al. (2010)
Licancabur M	Breakout	78	40	1.95	54	2.96	896	16.9	59.6	< 12	14	0.037	179	1.71	1.47	Figueroa et al. (2009)Mamani et al. (2010)
Licancabur S	Breakout	126	100	1.26	115	4.67	950	12.08	60.2	< 12	12	0.145	246	5.50	3.02	Figueroa et al. (2009)Mamani et al. (2010)
San Pedro W	Breakout	90	58	1.55	79	4.23	705	19.87	62.2	–	12	0.066	252	4.17	2.18	Bertin and Amigo (2019)
San Pedro SW	Breakout	111	58	1.91	38	3.94	903	22.9	62.02	15	12	0.029	155	0.85	1.78	–
Paniri	Breakout	99	57	1.74	97	3.54	1316	13.31	–	–	9	0.1	222	3.82	2.54	–
Lastarria N	Breakout	95	80	1.19	109	5.93	881	11.21	60.41	31	14	0.144	210	3.54	3.27	
Ollagüe S	Breakout	98	66	1.48	50	2.51	961	13.18	–	–	14	0.034	101	0.36	1.89	–
Olca Paruma W	Breakout	*	*	*	88	3.07	1190	18.29	63.52	30	14	0.096	284	6.38	2.6	Martinez (2019)
Falso Azufre W	Transitional	*	*	*	144	5.03	1876	13.84	–	–	8	0.208	235	4.41	5.19	–
Lascar S	Transitional	90	53	1.70	75	2.04	718	23.46	–	–	2	0.033	232	2.76	1.39	–
Ututuncu	Transitional	112	57	1.96	242	9.82	3781	11.34	65.64	35	14	0.971	244	15.27	19.2	Sparks et al. (2008)
Falso Azufre E1	Transitional	106	87	1.22	94	2.76	1231	10.19	–	–	5	0.109	162	1.70	2.92	–
Falso Azufre E2	Transitional	138	100	1.38	95	3.58	1795	9.37	66.8	–	3	0.147	122	0.76	4.81	Grosse et al. (2018)
El Misti	Transitional	120	66	1.82	118	3.51	720	24.38	60.5	–	5	0.064	304	25.79	2.13	Rivera et al. (2017)
Lastarria SW	Transitional	50	34	1.47	82	0.73	890	37.16	66.16	26	5	0.01	353	1.83	0.42	Naranjo (1992, 2010)
Aucanquilcha	Transitional	*	*	*	154	2.22	1208	32.81	–	–	4	0.088	169	0.50	1.67	
Llullaillaco S	Transitional	194	128	1.52	183	5.07	1649	22.28	65.65	17	14	0.28	576	208.18	4.52	Gardeweg et al. (1984)
El Muerto	Transitional	141	108	1.31	216	6.45	1809	10.76	–	–	4	0.413	218	29.70	8.67	–
Sairecabur S	Transitional	74	60	1.23	91	0.90	682	13.61	61.55	–	6	0.012	700	159.09	0.41	Mamani et al. (2010)

a Triangulated Irregular Network (TIN) surface from the mesh. The Delaunay criterion was applied to maximize the minimum angle of each triangle, avoiding the generation of narrow triangles (Dinas and Bañon, 2014). The recalculated pre-eruptive surfaces possibly present their maximum approximation in case of deeply channelized lava flows, a rather rare case for the selected dataset. Raster images with the pre-eruptive surfaces were generated from the TIN surface, and the average pre-eruptive slopes were measured along the central portion of the lava flows to avoid edge effects. The volume of a given lava flow was calculated as the 3D space enclosed by the modeled pre-eruptive surface and the present topographic surface within the lava flow boundary. Similarly, a thickness map was generated for each lava flow by subtracting the elevation of the pre-eruptive surface from that of the current topographic surface on a cell-by-cell basis. From these data, we computed the maximum thickness of each lava flow and the thickness along the axial profile.

We used the deviation from mean elevation (*DEV*) to qualitatively describe the topographic characteristics and roughness pattern of the lava flow surface (De Reu et al., 2013; Supplementary material 2). *DEV* measures the relative topographic position of a given cell x_0 by:

$$DEV = \frac{z_0 - \bar{z}_n}{\sigma_{z_n}} \quad (2)$$

where $z_0 = z(x_0)$ is the elevation at x_0, while $\bar{z}_n$ and σ_{z_n} are the mean elevation and the standard deviation of this parameter in the neighborhood of this cell, respectively. In this work, the bandwidth for this calculation was defined using a 5×5 matrix centered at x_0. A positive *DEV* value indicates that the cell is higher in elevation than the average of its neighbors, whereas a negative value means that the cell elevation is lower than the average elevation in the surroundings (De Reu et al., 2013). Typically, zones with high *DEV* values are recognizable as ridges, levees, or the vent area, while zones with negative *DEV* values are associated with areas close to levees and incisions alongside the front of the main ridges.

3.2.2. *Profiles derived from 8-bit grayscale satellite images*

Lava flows surface ridges and troughs are easily recognized from satellite images as they are shown as alternating dark and light bands due to regular variations in sun exposure and possibly variable weathering patterns. To assess the surface folding pattern, we introduced a spectral analysis of grayscale data obtained from satellite images (see section 3.2.3). To acquire this data, satellite RGB images (Fig. 1a) for each lava flow were downloaded from the Bing Maps satellite imagery repository with a resolution of 0.26 to 0.28 m/pixel. Satellite images were converted to 8-bit indexed color (Fig. 1b) through the median-cut color quantization algorithm (Heckbert, 1982) using Fiji, an open-source image processing package based on ImageJ (Schneider et al.,

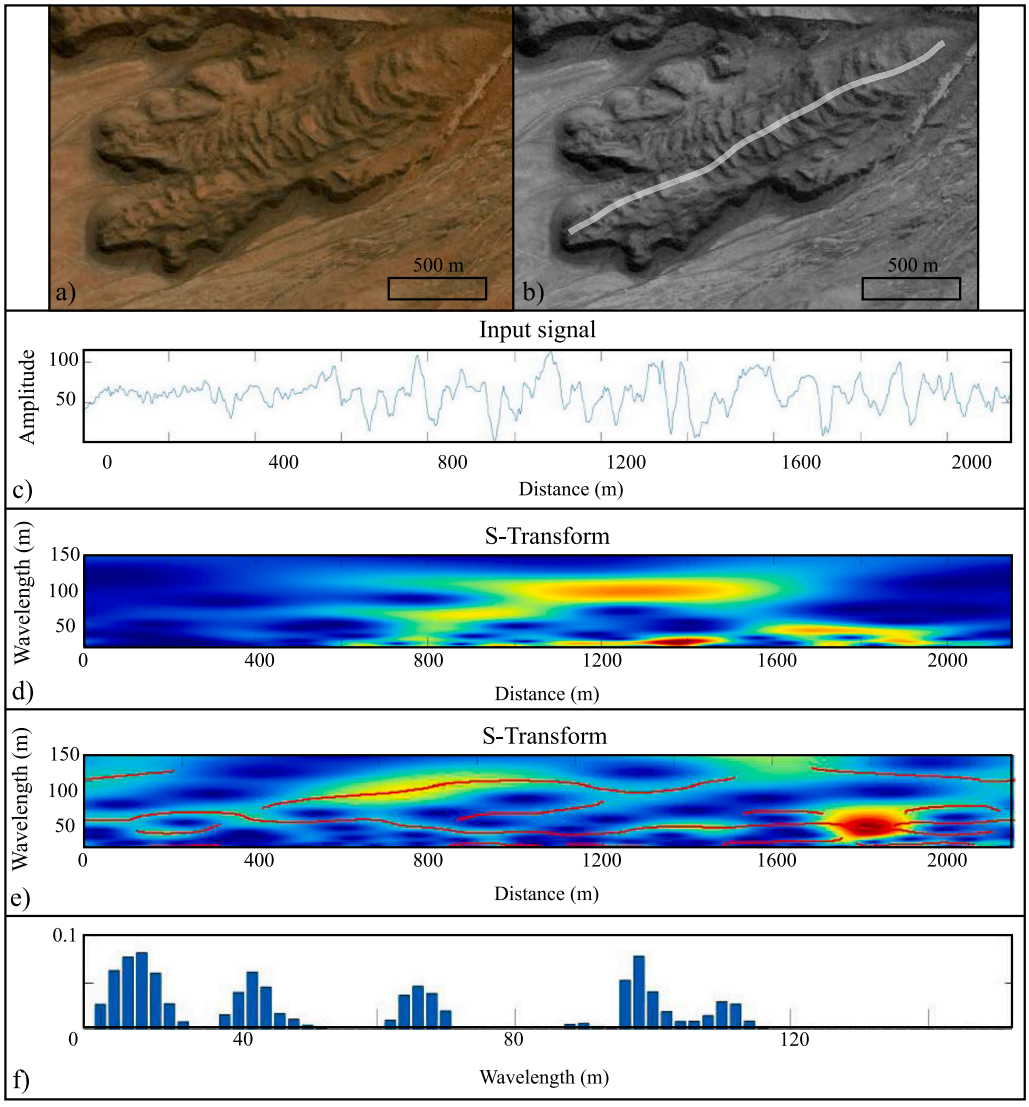

Fig. 1. Ollagüe S lava flow S-Transform spectral analysis. a) Satellite RGB image. Ridges are recognizable as structures transverse to flow direction. b) 8-bit grayscale image. Ridges are represented as black structures surrounded by lighter zones. The white line indicates the studied profile. c) Normalized and detrended grayscale-derived data measured along the surface profile. d) S-Transform spectral analysis. Dark red and yellow zones correspond to high coherence areas, while dark blue zones correspond to lower coherence areas. Coherence represents the quality of fit for a given wavelength (or frequency) at a given location. In other words, a high coherence zone identifies the presence of a dominant wavelength in the input signal at a given segment of the studied profile. e) Equivalent to panel d but including the identification of wavelengths with lateral continuity. f) Bar plot of the dominant wavelengths. (For interpretation of the references to color in this figure legend, the reader is referred to the web version of this article.)

2012). The brightness and contrast were adjusted to accentuate features like ridges, as they are observed as dark structures surrounded by lighter ones (Fig. 1b). In the grayscale image, each pixel contains intensity information (amount of light or shades of grays) from 0 to 255. Then, profiles along the flows were drawn, oriented orthogonal to the main structures (to crosscut alternating dark and light zones visible from the satellite images) along the central portion of the flow. The grayscale tone was measured along these profiles considering the mean values within an orthogonal window around the profile to reduce noise in the grayscale profile. The gray intensity measurements were obtained at regular steps throughout the profiles depending on the profile length, with steps varying between 0.96 m (e.g., Putana volcano) and 4.52 m (e.g., Chao dacite).

3.2.3. Spectral analysis and the S-transform

We analyzed the surface of the lava flows through a spectral analysis of the gray intensity profiles extracted from the 8-bit grayscale images. Surface structures can be in fact, clearly observed in satellite images as light intensity is primarily controlled by surface topography and, possibly, irregularities and weathering patterns. For this reason, the alternation of light and dark areas on the lava flow surface indirectly records the alternation of ridges and troughs on the lava surface, and the distance between two contiguous gray maxima (or minima) is a measure of the wavelength of these undulations.

To recognize the presence of repeating patterns along the profiles, we adopted a procedure similar to that described by Lescinsky et al. (2007), who analyzed digital elevation profiles along the flows using a localized Fourier transform, called *S-transform*. The S-transform is a spectral analysis method that allows determining the dominant frequencies locally in sinusoidal signals, thus providing useful information for identifying local structures and the wavelength of repeating patterns. This technique combines elements of wavelet transforms and short-time Fourier transform and has been widely adopted for spectral analysis (Stockwell et al., 1996; Stockwell, 2007).

Using this technique, Lescinsky et al. (2007) identified different classes of structures at the Medicine Lake dacite flow(Northern California, USA). A key difference between the technique presented by Lescinsky et al. (2007) and our procedure is the nature of the starting data. While Lescinsky et al. (2007) analyzed elevation data profiles, we studied gray intensity profiles derived from satellite images, focusing our analysis only on the wavelength of the observed light-dark alternations. This necessarily translates to some adaptations of the procedure, as described below.

For each lava flow, the starting dataset is represented by a profile with values of gray intensity sampled at regularly spaced nodes (Fig. 1c) on satellite images. First, following Lescinsky et al. (2007), detrending and normalization operations were applied to the profiles. This reduces monotonic variations of gray value due to variable luminosity within the satellite images. In particular, the detrending operation consists in subtracting a moving average function from the initial data. The window of this moving average is 700 m, which limits the maximum wavelengths that the procedure is able to identify in the studied lava flows. Note that the shortest lava flow analyzed is about 700 m-long, and thus this value allows us to apply a common detrending strategy for the whole dataset (obviously, the effect of the detrending operation in the shortest lava flows studied is negligible). Then, the S-transform is applied. This provides the local amplitude and local phase spectrum along the profile. The one-dimensional S-transform is named $S(x,\lambda)$, where x is the position along the profile and λ is the wavelength (additional details are presented in Lescinsky et al., 2007, and Stockwell et al., 1996). A high value of $S(x,\lambda)$ is suggestive of a dominant spectral component with a given wavelength λ at the position x along the studied profile. In other words, it suggests the presence of a dominant wavelength λ in the input signal at a given segment of the studied profile (around the position x). The resolvable wavelengths are equal to the profile length, 1/2 of the profile length, 1/3 of the profile length and so forth. Thus, spectral resolution is not uniform but increases as the wavelength decreases. We interpolated the values of the spectrum linearly to produce a uniform grid for $S(x,\lambda)$ in both directions (i.e., x and λ; Fig. 1d). Due to resolution limitations and boundary effects, we considered only wavelength higher than 20 m and lower than 1/5 of the profile length. We suggest that such limitation, given the scale of the observed surface structures as well as the general thickness, length, and width of the observed lava flows, does not reduce the ability of the method to identify and measure the first-order structures of the lava flows.

Because the absolute values of $S(x,\lambda)$ are also controlled by amplitude, they tend to be higher for structures characterized by long wavelengths. Thus, in addition to the absolute values of $S(x,\lambda)$, structure identification should consider the relationship between $S(x,\lambda)$ at a specific point and the surrounding values, which are characterized by similar wavelengths. Accordingly, considering fixed positions along the profile (x_i), our code selects all the relative maxima of the vectors $\overrightarrow{S}_{x_i} = S(x_i,\lambda)$, which are candidates to capture the wavelength of the dominant structures. From this operation, we obtain a set of positions (x_j,λ_j) which were clustered to identify continuous bands or patches with high values of $S(x,\lambda)$ and to discard isolated relative maxima, unable to capture the general characteristics of the flow (see Fig. 1e, where we illustrate the persistency of a given wavelength along the flow). Finally, considering only the identified maxima with lateral continuity (red lines in Fig. 1e), for each value of λ in the matrix $S(x,\lambda)$, we compute:

$$I_S(\lambda_0) = \sum_{j=1}^{N} S(x_j,\lambda_j)\varphi_{\lambda_0}(\lambda_j) \tag{3}$$

where $\varphi_{\lambda_0}(\lambda_j) = 1$ when $\lambda_j = \lambda_0$ and $\varphi_{\lambda_0}(\lambda_j) = 0$ when $\lambda_j \neq \lambda_0$. Thus, the function I_S is a measure of the relevance of the different wavelengths in the studied spectrum. Normalized bar plots show the smoothed results of I_S and allows identifying the dominant wavelengths in the grayscale profile (Fig. 1f).

3.2.4. Shape analysis of lava flow

To characterize and quantify the shape of the lava flow boundaries, we adopted a Fourier Descriptors (FD) method. The FD method has been widely used in biology, engineering, computer sciences, sedimentology, and paleontology to describe the shape of different objects. However, it has never been used to describe lava flows according to their morphology. The FD are obtained from the Fourier coefficients of a function that describes the shape of the lava flow outline as a polygon of N points $(x(a),y(a))$, with $a = 1, \ldots, N$. Each pair of coordinates is transformed in the complex number $z(a) = x(a) + y(a)\mathrm{i}$, and the FD coefficients $c(k)$ of the Fourier Transform of z are given by:

$$c(k) = \frac{1}{N}\sum_{a=1}^{N} z(a)exp\left(-2\pi i\frac{k}{N}\right), \quad k = 1,\ldots N \tag{4}$$

The $c(k)$ descriptors measure the frequency content of the curve. The first values of k describe low-frequency information and hence the overall shape of the object (in our case, the lava flow lobe), while higher frequencies record more detailed information about the high-frequency roughness of the object contour. A detailed description of the FD method is provided in Persoon and Fu (1977) and Glasbey and Horgan (1995).

Based on the Fourier Descriptors, we defined the variable $P(k)$ as:

$$P(k) = \frac{P_k}{P_0} \tag{5}$$

where P_k is the perimeter of the lava flow computed at a particular FD coefficient and P_0 is the real perimeter of the lava flow as measured directly on the satellite image. We performed the analysis from $k = 1$ until $k = 14$ for each lava flow. The value of $P(k)$ from 0 to 1, quantifies the perimetral complexity of the lava flow and increases monotonically with k. At a given k, lower values of $P(k)$ reflect a more complex shape of

the lava flow, while higher values of $P(k)$ typically reflect simpler external morphologies. To quantify the complexity of the lava flow outline, we selected the values of k at which $P(k)$ exceeds 0.95.

3.3. Lava flow viscosity modeling

The apparent viscosity was modeled for a subset of 14 lava flows with available information about composition and crystal content. Magma rheology does not depend only on the chemical composition of the melt, but also on the relative abundance and physical characteristics of the dispersed phases (crystals and bubbles). The apparent viscosity (η_{app}) of a polydisperse mixture of particles in a liquid phase is defined as a function of the viscosity of the melt (η_{melt}) and the relative viscosity (η_r) at a given particle volume fraction ϕ by:

$$\eta_{app} = \eta_{melt}\, \eta_r(\phi) \tag{6}$$

The viscosity of the residual liquid is controlled by temperature and composition. We calculated these parameters using the rhyolite-MELTS software (Gualda et al., 2012), trying to fit the known composition and crystallinity. The underlying assumption is that phenocrysts are formed in the magma reservoir at pre-eruptive thermodynamic conditions, whereas microlite crystallization occurred during magma ascent, eruption, and subsequent flow emplacement mainly driven by volatiles loss (Swanson et al., 1989; Cashman and Blundy, 2000; Chevrel et al., 2013). The bulk-rock composition was considered representative of the pre-eruptive composition in the magma reservoir, at 1 kbar, 2.5 vol% H_2O, and an oxygen fugacity controlled by a Quartz-Fayalite-Magnetite buffer. The crystallization of microlites was modeled using the residual melt composition and temperature by decreasing the pressure from 1 kbar to 1 bar under isothermal conditions (simulating magma ascent). The final isobaric crystallization stage is calculated at 1 bar from the liquidus temperature until the solidus temperature is reached. The assumption of a 2.5 vol% H_2O content may be an inherent limitation of the viscosity calculation; however, the presence of amphibole (typically observed in these lavas; e.g. Chao, Chac-Inca, Llullaillaco, Lastarria, Guallatiri, Uturuncu) indicates hydrous conditions, and the assumed water content is in agreement with that reported by De Silva et al. (1994) for the Chao dacite and in the range of glass inclusions from the Uturuncu volcano obtained by Sparks et al. (2008).

The viscosity of the interstitial melt was calculated following Giordano et al. (2008). This model was used because it has been successfully used for intermediate to silicic flows (Sato et al., 2013; Latutrie et al., 2017; Reyes Hardy et al., 2021) and, unlike to other viscosity calculators (e.g. Bottinga and Weill, 1972; Shaw, 1972), it considerers the non-Arrhenian T-dependence of viscosity by the Vogel-Fulcher-Tammann equation:

$$log\eta_{melt} = A + \frac{B}{T - C} \tag{7}$$

where A, B, and C are composition-dependant parameters and T is temperature (Giordano et al., 2008).

It is well-known that the relative viscosity η_r depends on the volumetric abundance, aspect ratio, crystal size distribution and shape of the crystalline phases, the strain rate of the flow, vesicularity, and bubble content (Castruccio et al., 2010; Cimarelli et al., 2011; Mueller et al., 2011; Chevrel et al., 2013; Klein et al., 2017, 2018). However, due to the lack of a robust dataset for the analyzed lava flows, we assumed a bubble-free interstitial liquid with bimodal crystal size and shape distribution.

The effect of the suspended phases was modeled as a mixture of coarse (ϕ_c) and fine (ϕ_f) particles (Farris, 1968; Chevrel et al., 2013) considering that:

$$\eta_r = \eta_r(\phi_c)\, \eta_r(\phi_f) \tag{8}$$

Coarse particles were modeled as spheres to mimic the effect of phenocrysts, while fine particles were modeled as needles to mimic the effect of microlites.

For calculating η_r, we adopted the rheological model proposed by Costa (2005) and modified by Costa et al. (2009), which is based on a semi-empirical non-Newtonian relationship for dilute-to-highly-concentrated polydisperse suspensions. We adopted this model because it considers the crystal fraction and shape of the particles and, contrary to other methods (e.g., Krieger and Dougherty, 1959; Pinkerton and Stevenson, 1992), it includes the strain-rate dependency that partially controls the geometrical redistribution of the suspended particles and the non-Newtonian behavior as:

$$\eta_r(\phi) = \frac{1 + \varphi^{\delta}}{[1 - F(\varphi, \varepsilon, \gamma)]^{B\phi_*}} \tag{9}$$

$$F = (1 - \varepsilon)\, erf\left[\frac{\sqrt{\pi}}{2(1 - \varepsilon)}\varphi\,(1 + \varphi^{\gamma})\right] \tag{10}$$

$$\varphi = \frac{\phi}{\phi_*} \tag{11}$$

where ϕ_* represents the critical solid fraction that indicates the transition from a system where the viscosity of the liquid phase controls the viscosity of the suspension to a system where particle-particle interactions induce a strong viscosity increase (Caricchi et al., 2007). The fitting parameters (Supplementary material 3) were extracted from Cimarelli et al. (2011) obtained from analog experiments of polydisperse suspensions of coarse and fine particles at an intermediate strain rate of 10^{-4} s^{-1}.

4. Results

Based on the general plain-view shape of the flows, thickness distribution, folding patterns, and the presence of distinctive morphological features such as levees, lobes, the position of the vent and surface textures, the 49 lava flows analyzed in this work were grouped into four main types: Ridged flows, Coulee lavas, Leveed flows, and Breakout flows (Fig. 2). A representative example is shown for each type of lava in Figs. 3-7, while all the analyzed flows and their data are presented in the Supplementary material 2. Lava flows with characteristics common to more than one type were categorized as Transitional lavas.

4.1. Ridged flows

This group comprises thick, large-volume lava flows with well-exposed and preserved arcuate ridges on the upper surface (Fig. 2a, 3a,c, Supplementary material 1.1). The flow surface is convex downflow, with long, continuous, and highly curved ridges that span the entire flow (Fig. 3a,c). Lava flow width tends to increase downslope, with the terminal front characterized by a single, sub-rounded lobe. Typically, thickness slightly increases downslope, with the maximum thickness (Table 2) located in the central sector of the channel (Fig. 3b, f). On gentle slopes, lava flows and the associated ridges are disposed nearly concentrically around the vent areas, while on zones with steeper slopes ridges only develop downslope.

In plain view, these flows show relatively simple shapes, with $P(k)$ exceeding 0.95 for values of k between 3 and 7. Typically, surface ridges present the longest dominant wavelengths (Table 3, Supplementary material 2.1), and they span the entire surface continuously (e.g., Bayo N, Ollagüe NW, Chao dacite, Acotango; Supplementary material 2.1) and have a direct relation with the maximum thickness (Fig. 3e and f).

4.2. Coulee flows

This group consists of lobulated lava flows with rough upper surfaces (Fig. 2b, 4a,c, Supplementary material 1.2). Widths and lengths tend to

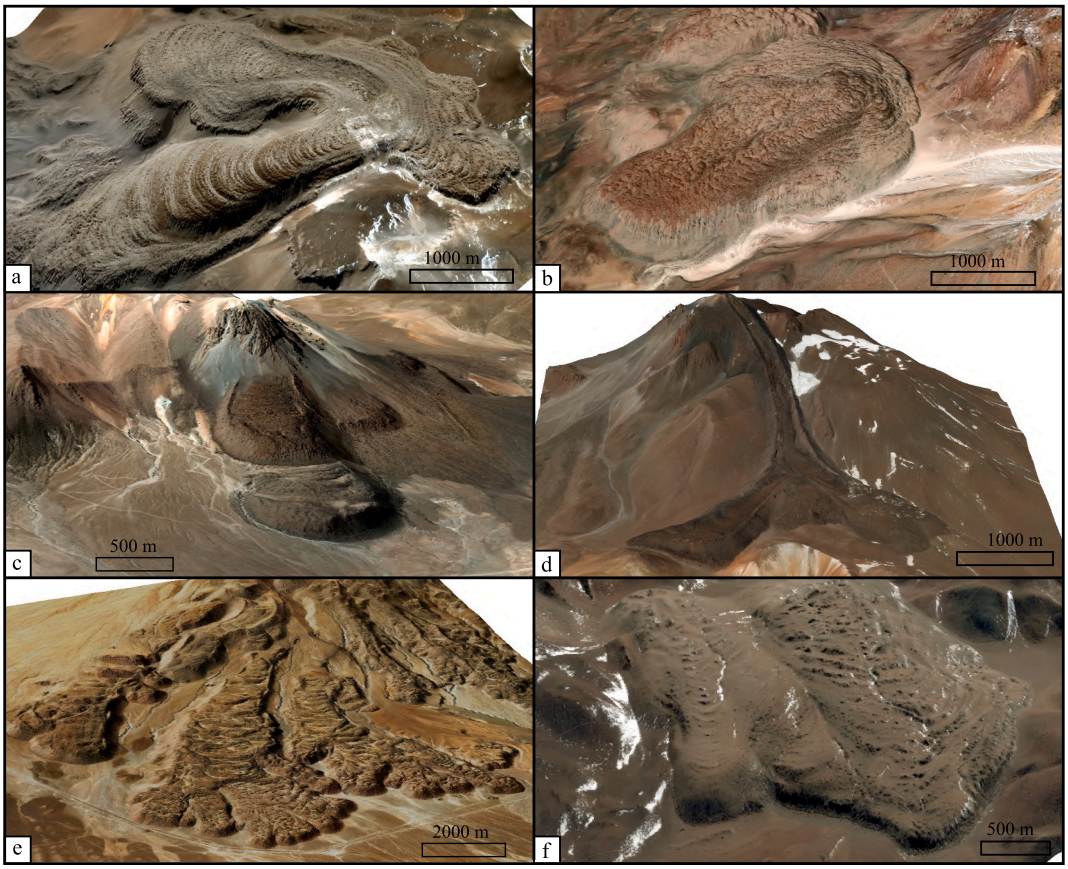

Fig. 2. Examples of the main types of flows identified in the CVZ. a) Ridged flow (Bayo N and Bayo S). b) Coulee flow (Chac-Inca W). c) Short leveed flow (Irruputuncu L and Irruputuncu U). d) Long leveed flow (Llullaillaco N). e) Breakout flow (San Pedro N, San Pedro NW, and San Pedro W). f) Transitional flows (Falso Azufre E1 and Falso Azufre E2).

be similar, while flow thickness progressively decreases downslope (Figs. 4b,f). These lavas are emplaced on medium slopes, with initial stages of growth associated with extrusion from a vent possibly sited on a sub-horizontal topography. Ridges in the vent area initially form continuous and concentric structures that progressively increase in width with distance. The ridges, which are convex downflow, are irregularly spaced and span the entire flow. They are generally laterally discontinuous, being mainly formed by the alignment of small, elongated mounds.

In plain view, these lavas exhibit simple morphologies, with *P* values above 0.95 at *k* values from 1 to 7. The maximum dominant wavelength of surface ridges typically occurs continuously only in medial sectors (Fig. 4e; Table 3, Supplementary material 2.2). The absence of a direct relationship between maximum thickness and maximum wavelength (Fig. 4e,f, Supplementary material 2.2) in this group may be due to an initial formation of concentric and tight ridges close to the vent area related to the extrusion itself. During lava emplacement, gravitational forces become dominant and control the propagation of the flow, extending the lava downslope with a subsequent elongation of surface ridges in this direction.

4.3. Leveed flows

This group corresponds to lava flows with rough surfaces, well-exposed levees that form a clear channel, and moderately preserved surface ridges (Figs. 2c,d, 5a,c). Maximum widths of these lava flows generally develop into the frontal sector, where they considerably exceed average flow widths. Thickness significantly increases downslope (Figs. 5b,f), generally reaching the maximum value at the flow front (Table 2). However, in some cases, thickness remains virtually constant downstream (Supplementary material 2.3).

Lava flows from this group present variable runouts. The underlying slope varies considerably between proximal (~34°) and distal areas (~14°) in long flows, while only steep slopes (> 30°) were observed in short flows (Table 2). Lavas are highly channeled, with well-formed levees in proximal-to-medial zones. Minimum channel width tends to decrease with slope. Surface ridges are moderately curved, convex to downflow, and span over the central portion of the flow channel. Generally, the ridges of long flows range from densely developed, regularly spaced ridges of decametric size and moderate curvature (medial-to-proximal zones; e.g., Olca-Paruma M, Supplementary material 1.3), to 100 m-height ridges, irregularly spaced, and with low curvature and density, which are recognized in medial-to-distal zones. In the shortest flows, the surface ridges are densely developed and are present along the entire flow.

In plain view, leveed flows show a simple shape, with P(k) values rapidly exceeding 0.95. Overall, short leveed flows have simpler shapes, reaching values of P(k) of 0.95 at k values from 2 to 3, while long leveed flows reach P(k) = 0.95 at *k* values from 4 to 7. The maximum dominant wavelength spatially correlates with thickness (Table 3). Lavas with thickness increasing downslope (e.g., Llullaillaco N, Falso Azufre M, Irruputuncu L, Llullaillaco U, Putana SW flows, Fig. 5, Supplementary material 2.3) present their maximum dominant wavelengths only on medial-to-distal sectors (Fig. 5e), while lavas without significant thickness variations show continuous dominant wavelenghts (Tata Sabaya volcano, Supplementary material 2.3).

4.4. Breakout flows

This group corresponds to lava flows characterized by a surface with

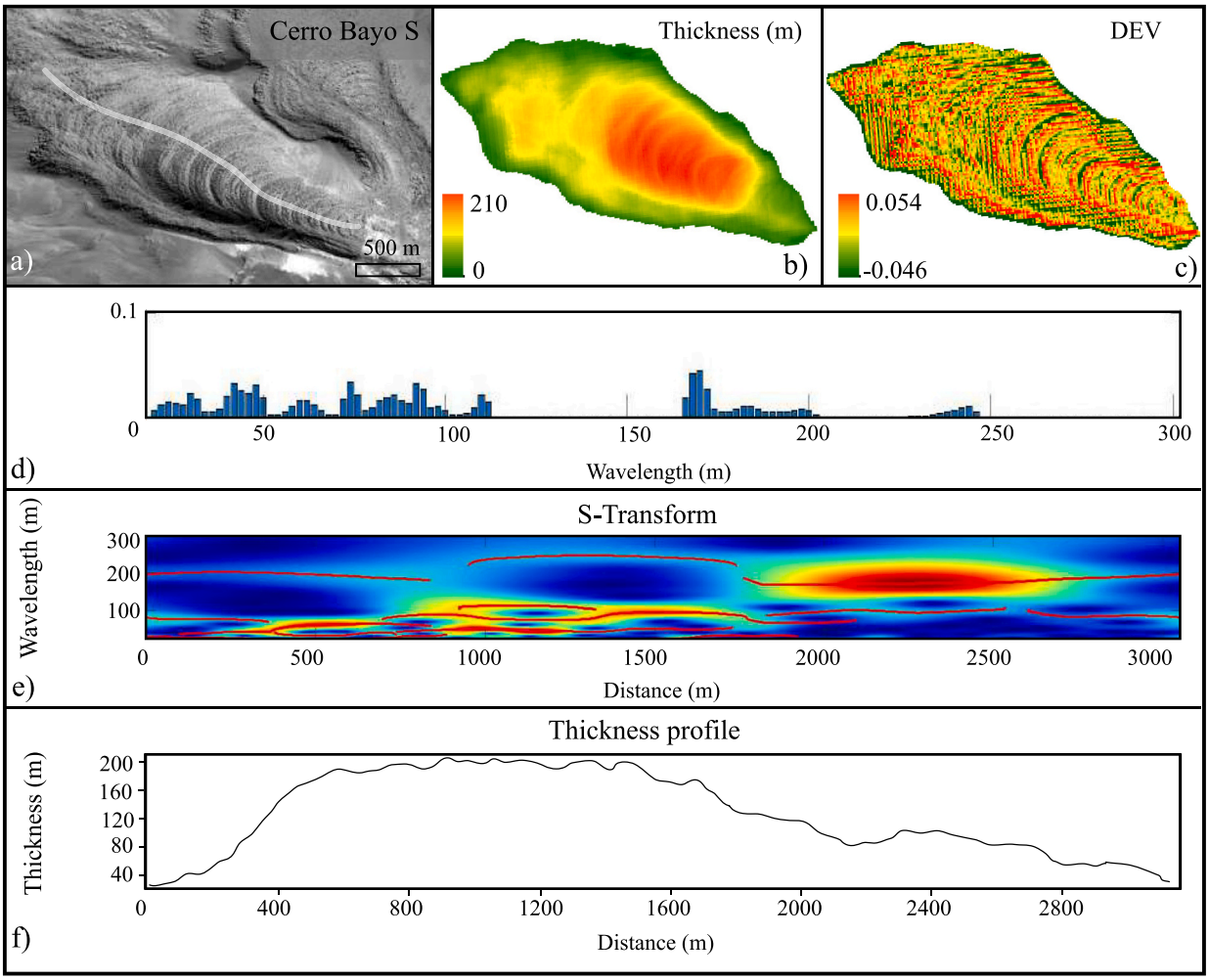

Fig. 3. Diagram with the analyses performed on the Bayo S ridged flow. a) the grayscale satellite image. b) thickness map. c) DEV map shows prominent ridges and steep edges as red zones. d) bar plot of the dominant wavelengths. e) S-Transform spectral analysis. f) thickness axial profile. The white line in the grayscale image represents the profile along which the spectral, thickness and slope analyses were performed. (For interpretation of the references to color in this figure legend, the reader is referred to the web version of this article.)

wide-to-braided ridges and multiple lateral and frontal lobes (Fig. 2e, 6a). In proximal zones, lateral margins vary from nearly linear to irregular with constant width, while flows enlarge toward distal areas, presenting multiple lobes and branched structures. These lava flows present discontinuous, narrow, and irregular levee structures that delimit a central channel, while convex ridges span the entire channel. Ridges are orthogonal to the flow direction, with irregular spacing and height. These lavas occur on gentle to medium slopes, and their morphologies and deformation patterns are not controlled by flow thickness.

Two families of breakout flows can be recognized based on thickness. Thick breakout flows have wide, straight, and cuspate ridges, generally spaced by deep troughs that span the entire channel width (Fig. 6a,c). The thickness (~ 130 m) does not significantly vary downslope, with maximum thicknesses and cuspate ridges generally occurring in correspondence with the central channel (Fig. 6b,f). In general, lobes are poorly developed and only occur as lateral structures. On the other hand, thin breakout flows have abundant, low amplitude and curved, braided ridges (Figs. 7a,c). Levee structures are common and more developed respect to thicker flows, while the maximum thickness (~ 75 m) tends to increase downslope (Figs. 6b,f). However, some of these flows also present virtually constant thickness with distance from the vent. Ridges show a braided aspect with breakouts and overflow widely developed along the lateral and frontal margins.

In plain view, these flows show the more complex morphologies, with P(k) values of 0.95 at *k* from 8 to 14. Overall, thin flows have more complex shapes than thick ones. Thin and thick breakout flows show a similar folding pattern, suggesting a direct relationship between thickness and the spatial distribution of the maximum dominant wavelength.

4.5. Transitional flows

Several lava flows exhibit morphological features intermediate between the different types (Fig. 2f, Supplementary material 1.5). This group includes lavas with variable morphologies, less marked surface patterns, and/or variations in the plan view shape characteristics, making it difficult to apply a univocal classification scheme.

Transitions between ridged and coulee lavas are recognized in two flows from the Falso Azufre volcano (Falso Azufre E1 and Falso Azufre E2 flows, Fig. 2f, Supplementary material 2.5). Conversely, other lava flows also show characteristic features of leveed and breakout lavas (Llullaillaco S flow, or transitional between breakout and short leveed flows (Sairecabur S flow). One small-volume flow from the Lastarria volcano (Lastarria SW flow) suggests a transition between coulee and breakout flows (Supplementary material 2.5).

4.6. General considerations on lava flow morphology

The variability of the morphological parameters typical of the

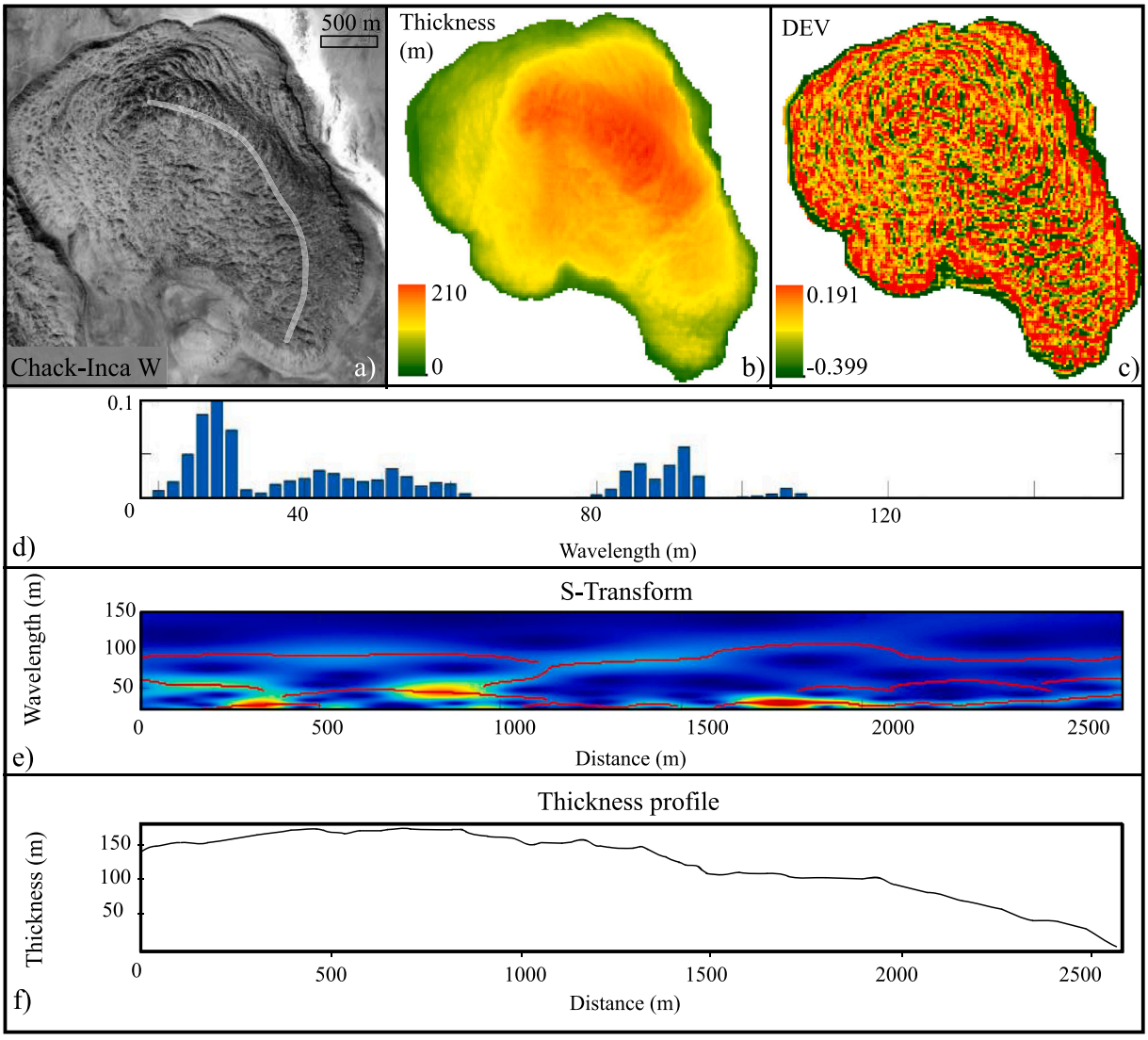

Fig. 4. Diagram with the analyses performed on the Chack-Inca W coulee flow. a) grayscale satellite image. b) thickness map. c) DEV map. Ridges and mounds are radially distributed around the vents, while they tend to be transversal to flow direction in distal areas. d) bar plot of the dominant wavelengths. e) S-Transform spectral analysis. f) thickness axial profile. The white line in the grayscale image represents the profile along which the spectral, thickness and slope analyses were performed.

different lava flows is well illustrated in Fig. 8, revealing for some of the flows a strict relation of the different types of lavas with some of these parameters. Transitional and ridged flows are present at different scales and are characterized by the largest variability of runout distance and invasion area (generally between 1 and 10 km^2, except for the ridged Chao dacite flow, which covers an area of about 60 km^2). Conversely, breakout and leveed flows are mostly dispersed over areas <3 km^2 and have maximum runouts between 3 and 6 km (Fig. 8a, b). The estimated medium thickness is always >15 m in all the lava types; thickness is generally very high (up to >100 m) in ridged flows, while leveed, breakout, and transitional flows have a modal thickness between 20 and 40 m (Fig. 8c). Leveed flows are on average emplaced over the steepest slopes (modal value of 32°) while coulee and breakout lavas are associated with slopes always lower than 24° (Fig. 8d). Slope and thickness information are combined in the calculated apparent shear stress responsible for the lava movement ($\tau_{app} = \rho \bullet g \bullet h \bullet \ sin\ (\alpha)$, where ρ is the lava density, g gravity acceleration, h thickness and α the slope angle). This parameter can be considered a rough, first-order approximation of the maximum value for the lava yield strength. More than half of the analyzed lava flows were emplaced under a τ_G lower than 400 MPa, with breakout flows having the lowest average values, while the highest τ_G values are associated with leveed and ridged lavas (Fig. 8e). Data on surface fold wavelength, although quite dispersed, show similar lower values for leveed and breakout flows (Fig. 8f), with the maximum wavelength positively correlated with the lava runout (Fig. 8g). Leveed and Breakout flows show more restricted widths than the other types, showing a linear relationship to thickness (Fig. 8h).

Results of plain-view shape analysis clearly demonstrate that leveed lava flows have the less complex morphologies, with P_k exceeding 0.95 for an average value of k of 4.1. Conversely, breakout lavas show the more complex shapes (mainly due to lateral and frontal lobes), with the lowest values of P_k that exceed 0.95 for an average k of 12.4. Ridged and coulee flows exhibit shapes with intermediate complexities (Fig. 9), as well as transitional flows (not shown).

5. Discussion

5.1. Effect of apparent viscosity

The mechanisms of lava flow folding and the resulting fold

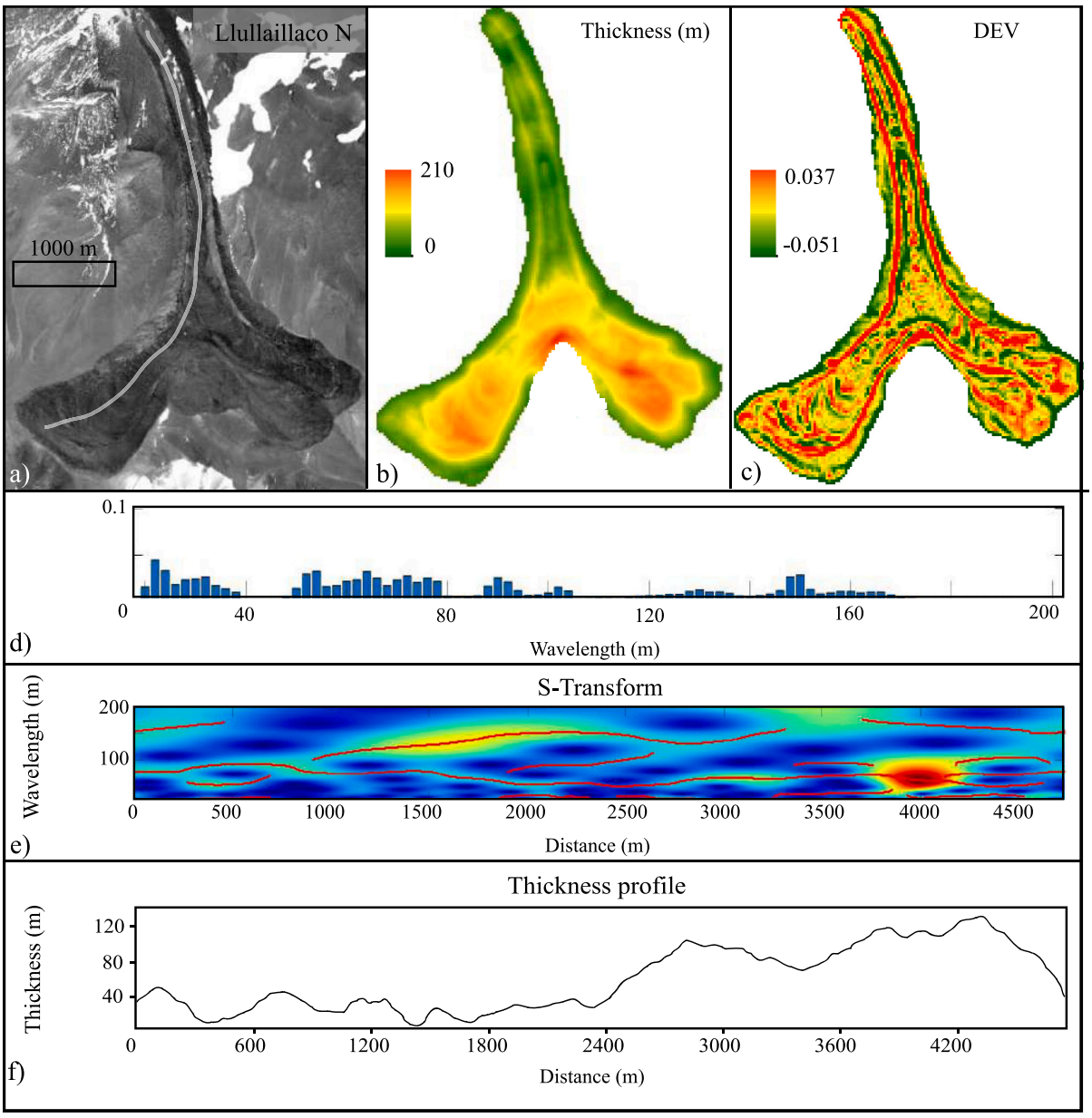

Fig. 5. Diagram with the analyses performed on the Llullaillaco N long leveed flow. a) grayscale satellite image. b) thickness map. c) DEV map showing levees and prominent ridges in the frontal zone clearly identifiable as high DEV zones. d) bar plot of the dominant wavelengths. e) S-Transform spectral analysis. f) thickness axial profile. The white line in the grayscale image represents the profile along which the spectral, thickness and slope analyses were performed.

wavelengths have been largely discussed in terms of their relations with compressive stress, thickness of the folded layer, vertical and horizontal gradients of temperature, lava viscosity and density (Fink and Fletcher, 1978; Fink, 1980; Lescinsky et al., 2007; Favalli et al., 2018). The maximum dominant wavelength has been used to constrain the thickness and viscosity of the folded layer and the compressive stress (Fink and Fletcher, 1978; Gregg et al., 1998; Castro and Cashman, 1999; Cashman et al., 2013; Deardorff et al., 2019). However, results from our morphological analysis show that the maximum wavelength of surface folds largely varies between the different lava types, with a correlation with lava runout and, to a lower extent, lava thickness.

A general relation links maximum wavelengths of folds and SiO_2 content, with basaltic flows characterized by small folds and wrinkles (generally <2 m in plain-view) while many evolved lavas present large, mesoscopic-scale ridge and through structures commonly interpreted as folds (Fink, 1980; Gregg et al., 1998; Cioni and Funedda, 2005; Deardorff et al., 2019). However, in the andesite-to-dacite range investigated in this study, the comparison between the maximum dominant wavelength and composition does not show a statistically significant correlation (Fig. 10a). This is consistent with previous data (Gregg et al., 1998; Pyle and Elliott, 2006; Lescinsky et al., 2007; Deardorff et al., 2019) and with the observed wide spectrum of lava morphologies within the restricted SiO_2 range considered here. This also translates into a poor correlation of maximum wavelength with lava viscosity (Fig. 10c). In fact, although the dataset spans a relatively restricted range of SiO_2, viscosities calculated for some selected flows (for which data on crystal content and bulk rock compositions are available) largely varies with SiO_2 (and corresponding crystal content) of the melt (Fig. 10b). Viscosity modeling returns a range of values that spans over 6 orders of magnitude (Table 4). Crystals are able to increase the melt viscosity by up to >5 orders of magnitude (Costa et al., 2009; Chevrel et al., 2013; Table 4; Fig. 10b), with the maximum values associated with coulee and ridged lavas (~10^{10}–10^{11} Pas; Table 4, Fig. 10b). However, the effect of crystals cannot be simply modeled by assuming a monodispersed population

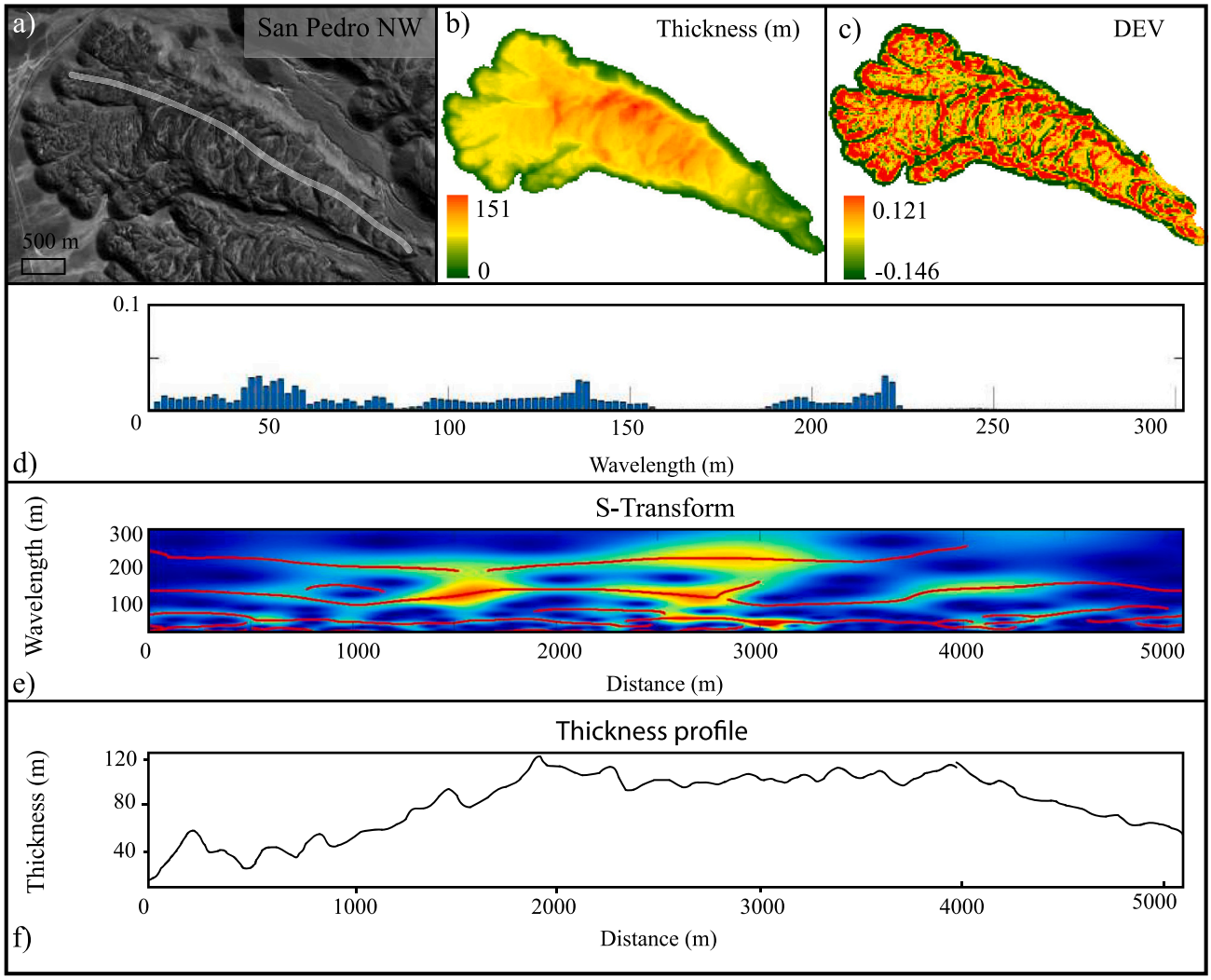

Fig. 6. Diagram with the analyses performed on the San Pedro NW thick breakout flow. a) grayscale satellite image. b) thickness map. c) DEV map showing prominent ridges, steep edges, and the intersection between breakouts mainly in the front. e) bar plot of the dominant wavelengths. f) S-Transform spectral analysis. h) thickness axial profile. The white line in the grayscale image represents the profile along which the spectral, thickness and slope analyses were performed.

(Cimarelli et al., 2011) because the maximum packing fraction increases with polymodality (Klein et al., 2017). Thus, phenocrysts and microlites do not have the same rheological effect. The presence of crystals also enhances the non-Newtonian behavior of lava flows, inducing shear thinning and viscoelastic effects (Caricchi et al., 2007; Castruccio et al., 2010; Mueller et al., 2011; Klein et al., 2017; Giordano, 2019). In general, the CVZ lava flows present a high-crystal content with rheology clearly approaching a non-Newtonian behavior (as testified, for example, by the formation of coulee or leveed lava flows). Calculated yield strengths vary in the range $\sim 10^4$–10^6 Pa (Hulme, 1974; Moore et al., 1978), suggesting that the flow advance could also be controlled by the onset of a core yield strength (Castruccio et al., 2013). While the value of the yield strength is not clearly correlated to any morphological parameter of the investigated lava flows, calculated viscosity shows a good positive correlation with the average lava flow thickness (Fig. 10d). This suggests that the effective viscosity may represent a first-order factor controlling the general thickness, and possibly, the runout of the lava flow.

Overall, thin, breakout lava flows (e.g., Licancabur volcano flows) present the lowest viscosities, with values of the order of 10^5 Pa s, while the thicker flows of the same category are crystal-richer and have viscosities 2–3 orders of magnitude higher (Table 4). The viscosity of channelized leveed lavas does not present significant differences between long and short flows, with values of about $\sim 10^6$ Pas. Coulee lavas are high-viscosity flows, with values of up to 10^{10} Pas, which is consistent with their morphological and emplacement characteristics similar to lava domes (Watts et al., 2002; Lescinsky et al., 2007). We obtained the highest apparent viscosity for the Chao dacite (ridged lava flow), which derives from the combination of its crystal-rich nature ($\phi_f > 0.3$) and high SiO_2 content. As expected, transitional flows exhibit an intermediate behavior.

5.2. *Other parameters controlling the morphology of the lava flows*

The observed relation between maximum surface fold wavelength and runout (Fig. 8g) clearly indicates the role of progressive deformation (and strain accumulation) in the build-up of these structures. The ratio Λ between the maximum wavelength and the second-maximum wavelength has been related to the relative rates of cooling at the flow surface and shortening by compression (Gregg et al., 1998), especially in the case of lava crust formation. This ratio varies between the different types of lava flows (Fig. 11a), with strictly similar average values for ridged flows and coulee lavas (1.42 ± 0.23 and 1.41 ± 0.28, respectively) and slightly different, higher values for the other three types (1.58 ± 0.24 for leveed flows, 1.55 ± 0.28 for breakout flows and 1.51 ± 0.26 for transitional flows). Although these values are slightly lower than reported

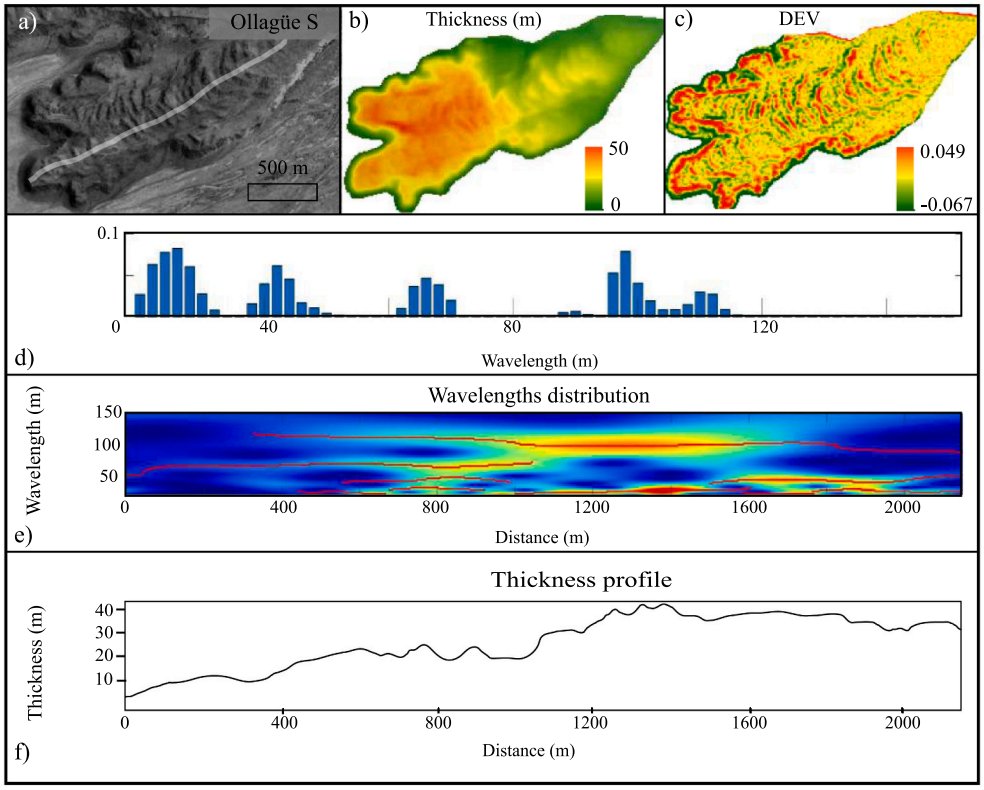

Fig. 7. Diagram with the analyses performed on the Ollagüe S thin breakout flow. a) grayscale satellite image. b) thickness map. c) DEV map showing prominent ridges, frontal and lateral edges, and braided areas as high DEV values. e) bar plot of the dominant wavelengths. f) S-Transform spectral analysis. h) thickness axial profile. The white line in the grayscale image represents the profile along which the spectral, thickness and slope analyses were performed.

Table 3
Main wavelengths identified using the S-Transform spectral analysis for the different types of lavas.

Type	First generations of folds	Second maximum dominant wavelength	Maximum dominant wavelength
Ridged	Intermittently along the flow surface	Continuous but not over the entire surface	Continuous along the entire surface. Spatially related to maximum thickness (90–274 m)
Coulee	Typically on proximal-to-medial sectors related to crumble breccias or spines	Discontinuously present along the entire surface	Continuously only in medial sectors (93–120 m)
Leveed	Discontinuous along the entire flow	Typically only in medium sectors	Spatially related to the thickness. Continuous on zone of maximum thickness (58–215)
Breakout	Discontinuous mainly in medial-to-distal zones	Spatially related to the thickness distribution.	Spatially related to the thickness distribution. Continuous along the surface for thick flows (98,285 m) and typically only in medial to distal zones for thin flows with a thicker front (74–111 m)

data (2.1 ± 0.3 for dacite lavas; 1.8 ± 0.4 for rhyolite lavas; Gregg et al., 1998), our results are quite consistent with previous studies that attempted to link Λ with composition (Gregg et al., 1998; Pyle and Elliott, 2006; Hunt et al., 2019; Farrell et al., 2018; Deardorff et al., 2019). The lava flows with the lowest values of Λ (ridged flows and coulee lavas; Λ close to 1.1 in Fig. 11b) are, in fact, associated with the largest apparent viscosity values and, hence, strain rates (Fig. 11b), while all the other lava flows have similar viscosities, nearly 3 orders of magnitude lower than the others (Fig. 11b). The low strain rates retard fold formation so that the difference between the two larger fold wavelengths is reduced.

Thickness and fold wavelengths, and their spatial distribution, can record the characteristics of the flow dynamics during emplacement. According to the different models of folding adopted (Biot, 1961; Fink and Fletcher, 1978; Castro and Cashman, 1999), the maximum dominant wavelength increases as a function of the thickness of the flow or of the rigid upper part of the lava flow (Fig. 12b). For example, Fink (1980) described fold formation in rhyolitic lava flows as related to the progressive growth of a rigid crust, in analogy with basaltic lavas (Fink and Fletcher, 1978; Farrell et al., 2018). Conversely, Cioni and Funedda (2005) described folds in crystal-rich comenditic lavas of Sardinia (Italy) as related to a process similar to the buckling of the entire thickness (>20 m) of the lava flow. In general, the lava thickness and the maximum dominant wavelength are not homogeneous along the surface of the flow, with maximum wavelength depending on the local thickness distribution and the flow type (Figs. 3-7). Overall, the highest values of thickness and wavelength occur in the central channel of ridged flows >100 m thick. In coulee flows, the maximum thickness occurs close to the vent area and is not directly related to the maximum wavelength distribution. Leveed flows show a unique downflow toe of maximum thickness and wavelength. Long leveed flows show longer maximum wavelengths than short flows, and the maximum wavelength for this type of flows shows a regular variation with their mean width (Fig. 12a). Similarly, breakout flows show a direct relation between maximum wavelength and mean flow width (Fig. 12a). In general, thin breakout

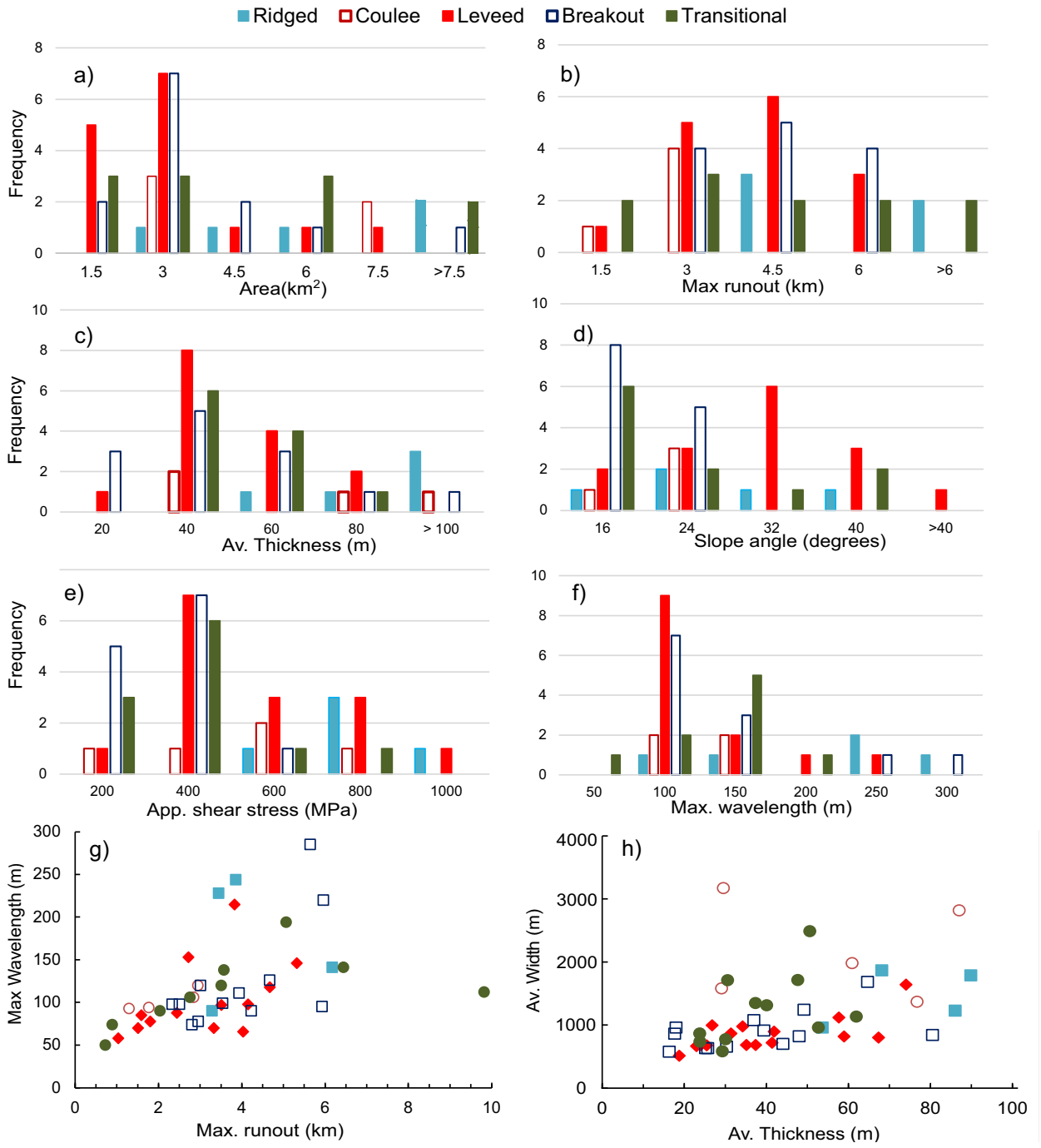

Fig. 8. a to f) Frequency histograms of morphological and dynamical parameters associated with the different types of lava flows. g) dependence of maximum wavelength of surface ridges on maximum runout. h) relationship between average thickness and width for the different types of lava flows (colors of symbols as for histograms).

flows have the lowest maximum wavelengths (Fig. 12b), while thicker breakout flows display higher maximum wavelengths typically developed more homogeneously and continuously along the central channel.

However, it is clear from our data that thickness alone does not fully control the folding pattern and that other factors (like flow width, runout or viscosity) can play a significant role in the resulting deformation pattern. In fact, thickness and runout are also governed by viscosity (Castro and Cashman, 1999; Griffiths, 2000; Castruccio et al., 2013), and thus both these parameters clearly control maximum wavelength formation (Fig. 10d). The dependence of maximum wavelength with lava runout (Fig. 8f) has already been discussed in terms of fold growth by progressive deformation during flow.

Volume and runout of lava flows are quite closely related (Fig. 12c), with larger flows reaching the maximum distances. The four lava flow types here defined depict good trends between these two parameters, with breakout flows typically associated with larger runouts, and coulees with smaller runouts, for a given flow volume. Ridged flows have on average large runouts and the largest volumes (with up to >9 km of runout and 10 km^3 of volume for the Chao dacite, not shown in Fig. 12c). The Cerro Uturuncu lava flow, classified as transitional due to the presence of a ridged surface and marginal levees and a lateral lobe, reaches a runout of near 10 km, plotting on the same trend of ridged

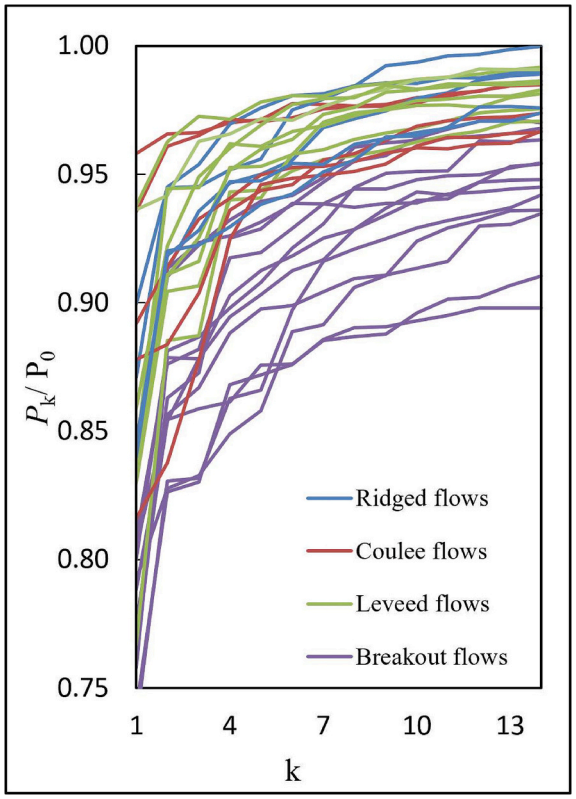

Fig. 9. Plot of k values vs P_k/P_0. Initial low values of P_k/P_0 and steep slopes correspond to plain-view complex morphologies, while relatively gentle initial slopes that rapidly flatten indicate simple shapes. Transitional flows are not included to avoid overlapping.

lavas.

The maximum thickness observed for the different lava flows is strictly related to the mean thickness (calculated as the ratio between the calculated volume and measured area of the lava flow). Therefore, we suggest using the very good correlation between these two values (Mean thickness/Max thickness = 0.3645; Fig. 12d) for a first-order calculation of lava flow volumes from measurements of the lava flow area and observed estimated maximum thickness.

5.3. The role of the pre-eruptive surface slope

The pre-eruptive slope is one of the most important control parameters for maximum runout of mafic lava flows (Walker, 1967; Hulme, 1974), together with other important factors such as viscosity and effusion rate (Walker, 1973). Conversely, the intermediate to silicic lava flows studied here show a very weak dependence of runout with the slope, with significant scattering for all the lava types, suggesting a dominant effect of other parameters (Fig. 13a). In general, for a given effusion rate and initial viscosity, lava flows emplaced on steeper slopes are longer and faster. However, it is crucial to consider the flow type when interpreting flow length (Walker, 1973; Gregg and Fink, 2000; Harris and Rowland, 2009). Branching, and consequently lava flow morphology, are partially controlled by the slope as it impacts the thickness, width, and flow advance rate (Dietterich and Cashman, 2014). In the CVZ, branching is a distinctive feature only appreciated at a scale of flow segments in medial and distal areas of breakout flows over a low slope. Typically, the slope exerts an important control on flow thickness, such that lava flows thicken on low slopes and thin on steep slopes (Lister, 1992; Griffiths, 2000; Gregg and Fink, 2000; Dietterich et al., 2015). However, considerable overlapping occurs in thickness values in flows emplaced on 10–25° surfaces (Table 2), suggesting that thickness is mainly controlled by other factors (e.g., viscosity, mode of deformation) with reciprocal, not linear, relationships.

On the other hand, data from Table 2 suggest a significant effect of average slope in controlling the maximum thickness of the flow. The maximum thickness of leveed lava flows tends to increase with slope, while thickness of ridged lavas shows an inverse correlation. Conversely, the maximum thickness of coulee and breakout lava flows appears nearly independent from the slope. We suggest that these very different behaviours derive from the combined effect of lava viscosity and effusion dynamics (see section 5.5).

Regarding lava width, this parameter may be primarily controlled by the characteristics of the underlying surface (Hulme, 1974; Lister, 1992; Kerr et al., 2006; Dietterich and Cashman, 2014; Richardson and Karlstrom, 2019). Flows are narrower on steeper slopes, generally enlarging into wider, fan-shaped zones on distal areas. Flow width is determined by the competition between cross-slope flow spreading and lava cooling or crust formation (Cashman et al., 2013). The larger widths are observed in ridged and coulees flows or in some transitional lava flows, while minimum values occur in strongly channeled leveed and thin breakout flows (Figs. 8h, 12a).

As a matter of fact, the control of viscosity and, to a variable extent, of pre-eruptive slope on thickness, together with effusion rate, govern the dynamics of the flow, affecting flow velocity and directly impacting different morphological features such as runout, width, and general deformation dynamics. This is suggested by the roughly positive relationship between the maximum wavelength of flow deformation and the gravitational component of the shear stress τ_G applied to the lava flow (Fig. 13b). This suggests that thickness and slope, and hence other related parameters such as emplacement velocity, may partially control the folding process. For example, the presence of breaks in the slope of the underlying surfaces may control the distribution and continuity of the different wavelengths along the flow path, as the spectral analysis shows a positive correlation between changes in the pre-eruptive surface and the influence area of minor wavelengths (see Supplementary material 2).

5.4. Effects of breaks in slope

The occurrence of breaks in slope at a local scale, depending on the local slope and the flow rate, may impact lava flow width, thickness, and branching (Dietterich and Cashman, 2014; Harris and Rowland, 2015). The different types of lava flows present a systematic correlation between lava thickness upstream or downstream from a break in slope, while no clear relationship between thickness and steepness of the break in slope is recognized. In general, the lava flows adjust thickness to the new slope after a break in slope. Most flows thicken as slope flattens; ridged flows have the largest thickness increase even with small changes in the slope, although some flows (e.g., Acotango, Chao dacite, and Ollagüe NW) present a thickness decrease after the slope flattening (Fig. 14). Only a few lava flows develop slightly thicker zones as they pass to steeper slopes (Fig. 14). Additionally, coulee lavas show a general decrease in thickness with distance, independent of the slope break. The thickness decrease with slope flattening observed for ridged and coulee lavas suggests a prominent role of viscosity increase with distance, which slows down (or stops) the increase in thickness of the lava front.

Conversely, the very large thickening (up to >100 m; Fig. 14) of some ridged flows suggests a long-lasting high mobility of the lavapossibly related to high effusion rates. Leveed lavas are characterized by a nearly ubiquitous increase in thickness with a flattening slope, suggesting continued flow mobility after levee formation, so resulting in the partial drainage of the channel (Borgia and Linneman, 1990; Naranjo et al., 1992; Harris and Rowland, 2009; Cashman et al., 2013). Similarly to basaltic lavas, the development of the channel could, in fact, result in a general velocity increase to comply mass conservation, which possibly explains the generally large runout of these flows despite their small

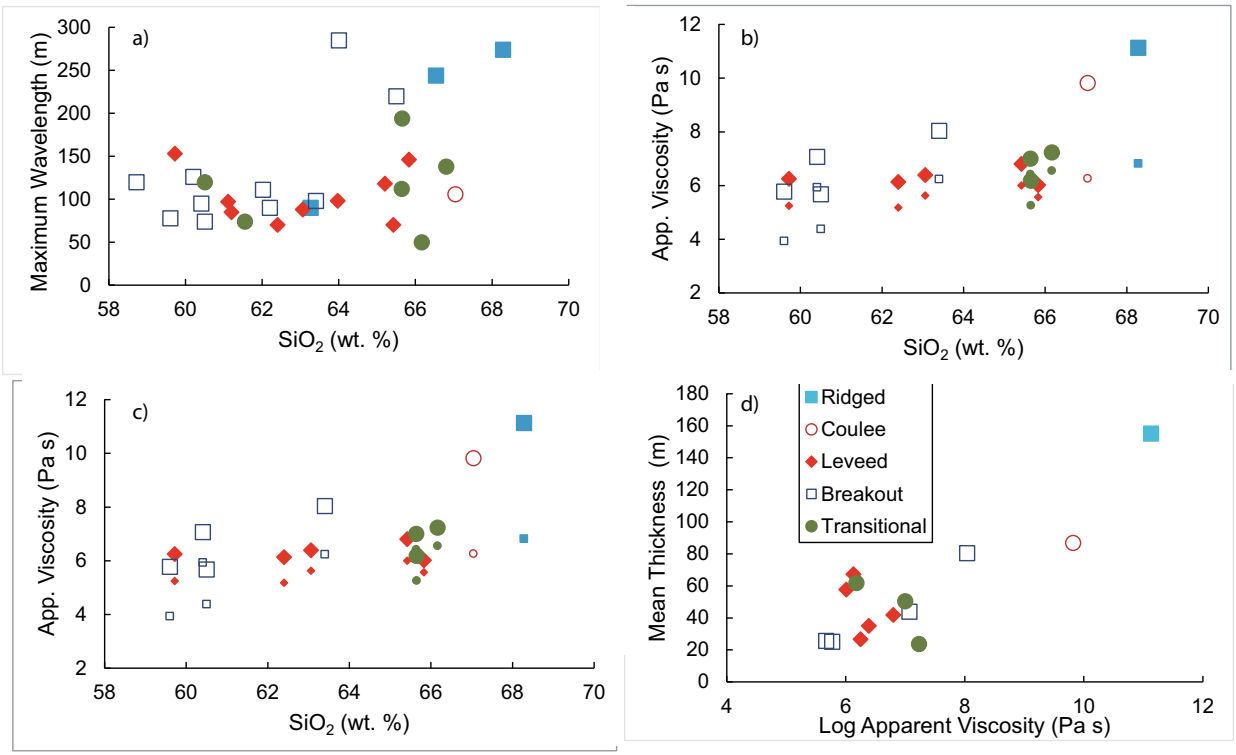

Fig. 10. a) Composition vs. maximum wavelength shows a poor correlation, with significant overlapping between the different lava groups, especially in the range 64–67 SiO_2 wt%. b) Large symbols represent the calculated apparent viscosity of the lava, while small symbols indicate only the viscosity of the residual melt (n_{melt}). The effect of crystals induces a sharp increase in the apparent viscosity (up to 5 orders of magnitude). Note that flows with higher SiO_2 contents may present lower apparent viscosity than more crystalline and less evolved lavas. c) Apparent viscosity vs. maximum wavelength shows a poor correlation. Despite the broader range of viscosities for breakout flows compared to leveed flows, they present more restricted maximum wavelengths, suggesting that the maximum wavelengths in leveed flows may be strongly ruled by other parameters such as effusion rate. d) Plot of the apparent viscosity vs. the mean thickness shows a positive correlation, suggesting that the dynamics of ridged and coulee flows, and to a lesser extent of thick breakout flows, may be strongly controlled by their high viscosities.

Table 4
Melt, relative, and apparent viscosities for the CVZ lava flows with available composition and crystallinity. n_{melt}: liquid viscosity, n_r: relative viscosity, n_{app}: apparent viscosity.

Flow	Type	Log(n_{melt}) Pa s	Log(n_r) Pa s	Log(n_{app}) Pa s
Chao dacite	Ridged	6.82	4.31	11.13
Chac-Inca W	Coulee	6.26	3.56	9.82
Irruputuncu U	Leveed	5.18	0.95	6.13
Irruputuncu L	Leveed	5.24	1.01	6.25
Llullaillaco U	Leveed	6.00	0.80	6.80
Llullaillaco N	Leveed	5.57	0.44	6.01
Olca-Paruma M	Leveed	5.62	0.77	6.39
Lastarria N	Breakout	5.93	1.14	7.07
Licancabur N	Breakout	4.38	1.29	5.67
Licancabur M	Breakout	3.93	1.84	5.77
Guallatiri	Breakout	6.24	1.80	8.04
Uturuncu	Transitional	6.42	0.58	7.00
Llullaillaco S	Transitional	5.26	0.92	6.18
Lastarria SW	Transitional	6.55	0.68	7.23

volume (Hulme, 1974; Pinkerton and Wilson, 1994; Glaze et al., 2009) (Fig. 12c). Breakout flows do not show significant thickness variations with slope changes. The small thickness increase (about 10 m) with steepening shown by some flows is possibly comprised within the error in thickness estimation (derived from the difference between the present topography and the reconstructed basal surface of the lava). The general effect of breaks in the slope of the basal surface seems to result only in thickness changes at the local scale, without determining downflow changes in the other characteristics of the lava flow. Lev et al. (2019) performed experimental analyses and investigated the direct effect of the slope breaks on the flow velocity. They demonstrated no predictable inheritance of channel width with a steepening or shallowing of the underlying bed, with only a direct relationship between slope and flow velocity.

5.5. Eruption conditions

This proposed differentiation of lava flow types, mainly based on their surface morphology and shape characteristics, produces significantly overlapped groups when other descriptive parameters are considered (Fig. 8). This may be attributed to our limited knowledge of the emplacement conditions for flows of intermediate to silica-rich compositions (Deardorff and Cashman, 2012; Tuffen et al., 2013; Deardorff et al., 2019) due to their infrequent occurrence and only sparse (or absent) real-time observations. Observations are mainly limited to andesitic leveed lava flows (Borgia et al., 1983; Naranjo et al., 1992; Navarro-Ochoa et al., 2002; Harris et al., 2002; Wadge et al., 2014). Although rhyolitic, the well-described 2011 lava of Cordon Caulle (Chile; Tuffen et al., 2013; Farquharson et al., 2015) can be classified as a breakout/ridged flow. For this reason, source parameters controlling the emplacement of silicic lava flows are poorly constrained by direct observations, and analysis of morphological and rheological features of past lava flows remains the only method to define at least the range of their variability. Numerical models for estimating parameters such as the effusion, cooling, and crust growth rates often require several assumptions that may increase the uncertainty. In particular, several methods have been proposed for estimating effusion rates and other rheological parameters of basaltic lavas from their observation (among others, Jeffreys, 1925; Pinkerton and Sparks, 1976; Kerr et al., 2006; Harris et al., 2007; Harris and Rowland, 2009). In addition, the results of these calculations are often typically underestimated, resulting in

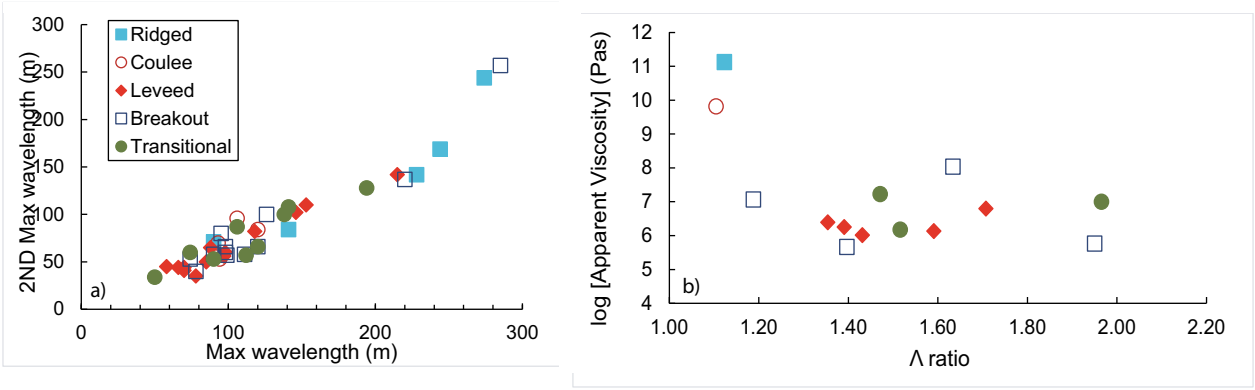

Fig. 11. a) Maximum wavelength vs. the second maximum wavelength. A linear relationship is observed between wavelengths in the range 50–250 m. b) Λ vs. apparent viscosity. Two main groups are identified: one group with variable Λ values and viscosities in the range 10^6–10^7 Pa s^{-1}, and the other with small Λ and n_{app} that exceed 10^8 Pa s^{-1}.

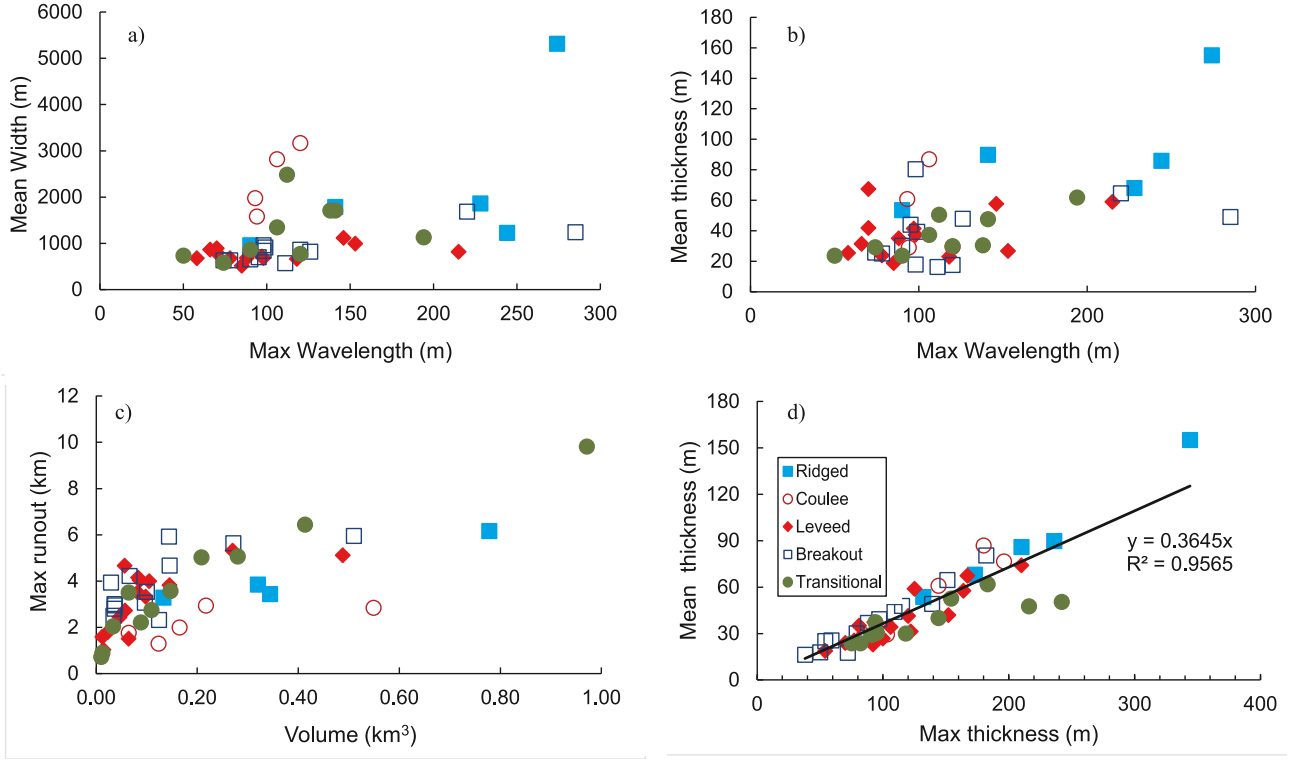

Fig. 12. a) Maximum width vs. mean wavelength. Coulee flows do not show a good correlation, suggesting that other parameters, such as thickness, may control the maximum wavelength. On the other hand, Leveed flows show a good correlation between maximum wavelength and mean width. b) The maximum wavelength increase as a function of the flow thickness. Ridged flows have the highest values suggesting a strong control of thickness in folding. c) Volume vs. maximum runout shows a positive correlation as the final volume depends on the eruption time and the effusion rate (that partially controls the runout). Larger flows reach longer distances; however, the overlap is significative at low volumes, with coulee flows showing the lowest runout at a given volume. d) maximum thickness vs. mean thickness shows a very good positive correlation with mean thickness/Max thickness similar to 0.3645.

average values which do not consider the temporal fluctuations or variations of these parameters (Naranjo et al., 1992; Navarro-Ochoa et al., 2002; Pallister et al., 2013; Bertin et al., 2015).

Using an experimental approach, Lyman et al. (2004) proposed that eq. (1) reported at section 2.2 could be used to predict effusion rates Q_e of silicic lava flows and domes starting from their morphological features. Under the approximation of σ_0 as derived from lava morphology, we calculated the theoretical Q_e of all the studied lava flows (Table 2 and Fig. 15a).

Effusion rate well correlates with lava volume for the different types of lava (Fig. 15a) and, unexpectedly, only to a lower extent with runout distance (Fig. 15b). Larger volume lavas generally correspond to higher Q_e, with leveed and ridged lavas being emplaced more rapidly (over times of a few days) than the other lava flows. Ridged lavas also present high, poorly variable effusion rates, with Q_e generally larger than 100 m^3s^{-1}. Effusion rates of breakout lavas and coulees are lower and span over about 2 orders of magnitudes, which translates into effusion durations between months and a few years (Fig. 15a).

Ridged and coulee flows have different characteristics that are possibly modulated both by the effects of largely different effusion rates (Fig. 15a) and similar rheology. Coulee flows have transitional features between high-viscosity lava flows and domes. They resemble the lobate

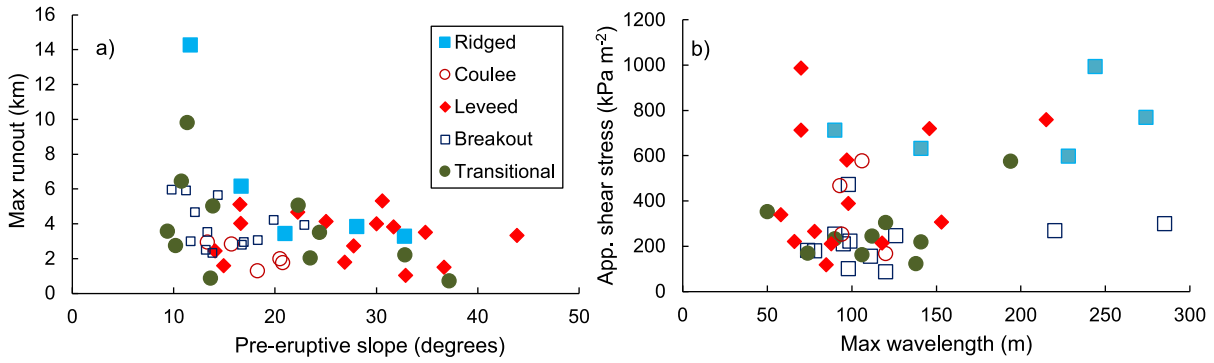

Fig. 13. a) Pre-eruptive surface slope vs. maximum runout. This plot shows significant overlapping between the different lava types, suggesting that the pre-eruptive topography by itself may only exert a minor control in the runout distance of the CVZ lavas. b) Maximum wavelengths vs. apparent shear stress. This plot suggests that a combination of thickness and slope may control the folding process. Coulee lavas have a more restricted range of dominant wavelengths with variable τ_G, and ridged and breakout lavas have broad ranges of dominant wavelengths, despite presenting high and low τ_G values, respectively.

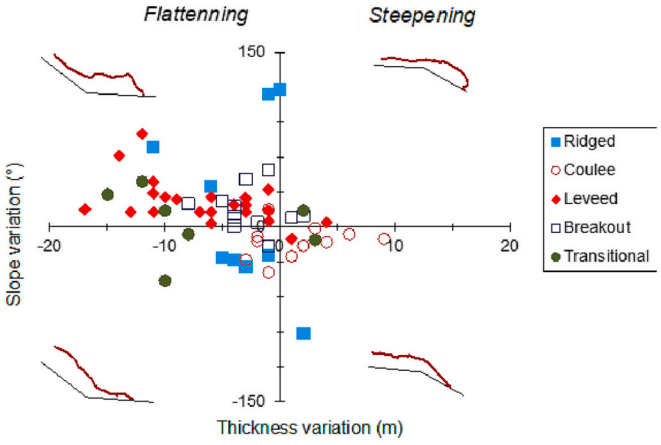

Fig. 14. Diagram of thickness variation concerning breaks in slope. The upper left and lower right areas correspond to the expected behavior of thickness to changes in the underlying slope, while the other areas represent zones of inheritance (they have unexpected thickness variations as they decrease in thickness on more flattening surfaces and vice versa). All coulee flows decrease in thickness independent of the slope, while leveed flows show the expected behavior in response to variations in the slope, typically increasing in thickness to downslope. Some ridged flows suggest inheritance as they decrease in thickness as they flatten. Breakout flows do not show significant inheritance.

to platy morphologies obtained experimentally by Fink and Griffiths (1998) and Lyman et al. (2004), which derive from low eruption rates. Coulee lavas are emplaced on gentle to medium slopes with initially radial growing due to inflation of the solidified crust (Griffiths and Fink, 1997), while as the volume increases, the gravitational forces become significant, inhibiting a general thickening and starting to spread the flow laterally (Lescinsky et al., 2007). Flow emplacement possibly occurs over a long period, of the order of up to several years.

Elongated ridged flows may be emplaced with higher effusion rates and underlying slopes (De Silva et al., 1994) than coulees. While for basaltic lavas, thermal insulation is efficiently produced by the formation of a thick crust (Harris et al., 2002; Bullock et al., 2018), the high flow rate of these highly viscous flows contributes to rapidly increases their thickness, so minimizing heat losses. As a result, the flow may advance further (Fig. 12c) before cooling becomes a substantial factor forcing stagnation (Fink and Griffiths, 1998; Harris et al., 2002; Magnall et al., 2017).

Leveed flows have a channeled nature, which, together with steep initial slopes (> 30°), strictly agrees with the calculated high effusion rates (Walker, 1973; Fink and Griffiths, 1990; Gregg and Fink, 2000; Harris and Rowland, 2009) and the low, restricted values of viscosity (Fig. 10, Table 4). The advance rate of these flows and the gradient between steep proximal zones and more flat toes may induce high stress to the surface crust flow (Kilburn, 2004; Magnall et al., 2017), triggering a more regular disruption as testified by the rough surface with small blocks (Leggett et al., 2020). The generally low volume fraction of microlites of this type of lavas suggest rapid magma ascent, extrusion, and emplacement (Cashman and Blundy, 2000; Watts et al., 2002). These flows strictly resemble the levee flows experimentally obtained by

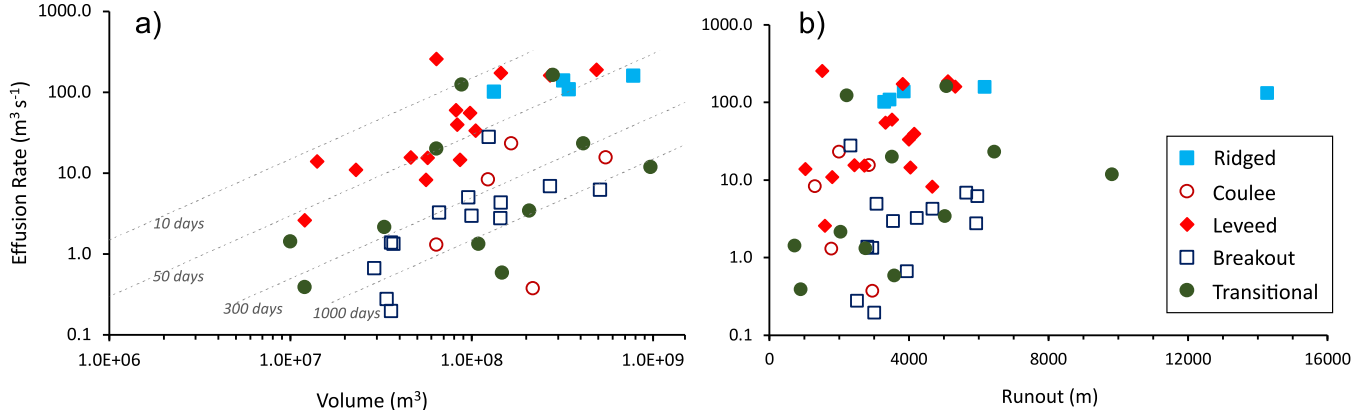

Fig. 15. a) Volume of the different lava flows vs. effusion rate. Hatched lines are isochrones. b) Runout of the different lava flows vs. effusion rate. Different lava flows show a poor correlation.

Gregg and Fink (2000), who clearly demonstrated that they are formed under conditions of low cooling (made easier by the generally high thickness; Fig. 15b) and high effusion rates.

Breakouts and overflows typically of breakout flows (and some transitional flows) arise when the flow halts and the lava is continuously supplied, resulting in inflation and increased internal pressure (Calvari and Pinkerton, 1998). As the pressure exceeds the local confining force, a rupture of the surface crust or the levees occurs, redirecting the flow and forming new lobes (Pinkerton and Sparks, 1976; Farquharson et al., 2015; Magnall et al., 2018). This process may cause lower thicknesses of thin breakout lavas, as it can divide the lava flux into multiple branches reducing the flow thickness and the flow advance rate (Lister, 1992; Dietterich and Cashman, 2014; Magnall et al., 2018). Breakouts can be formed due to oscillations in the effusion rate, which propagate an increased supply of lava to the flow front or along the flow margins (Dietterich et al., 2012; Magnall et al., 2017). These processes have been well described for the 2011–2012 Cordon Caulle eruption, where the morphology changed from a simple to compound flow with lateral lobes 64–116 days after the eruption started. This morphology change occurred during a phase of general decrease of the effusion rate (10–20 m^3s^{-1}; Bertin et al., 2015) that followed the initial phase of effusion rate (50–70 m^3s^{-1}; Bertin et al., 2013), reflecting a progressive stagnation of the flow fronts and margins (Tuffen et al., 2013). As demonstrated by the Cordon Caulle lava, emplacement of breakout flows can occur over long periods, which supports the average low effusion rates calculated for this lavas in the CAVZ (Fig. 15a).

5.6. Morphology-based characterization of intermediate blocky lavas

We performed a systematic morphological and morphometrical characterization of intermediate to silicic lava flows, evidencing four main types. This division is based on descriptive elements including the presence of particular features such as lobes, levees or types of ridges, the shape of the flow and a set of morphometrical data. A correct characterization with a consistent application of these proposed types may allow us to link the different flows of similar characteristics with their common dynamics and emplacement mechanisms. Lava flows with characteristics related to more than one group are also considered here and generically defined as Transitional lavas. As for pahoehoe to blocky lavas, intersections between the different morphologies are common and may be related to fluctuations of the complex eruptive dynamics during lava flow emplacement.

As we discussed in the previous sections, the morphology of these lavas is not controlled by a single parameter, being generally the result of the combined effects of the topography, rheological properties of the magma, and effusion rate. We categorized in a schematic illustration (Fig. 16) the different types of lavas here identified as a function of the η_{app} and the effusion rate, although we demonstrated also a clear role of topography and pre-eruptive surface slope. In general, leveed and ridged lavas might be formed under high effusion rates but with contrasting viscosities (Table 4). On the other hand, breakout and coulee lavas also have contrary rheologies, but they are formed under low effusion rates. Transitions between types with similar rheology are common (e.g., Llullaillaco S, breakout to leveed flow; Falso Azufre E1, coulee to ridged flow). Conversely, transitions between lavas types with different viscosities are less frequent. They may occur related to crystal-rich thick breakout flows (e.g., Uturuncu, Breakout to Ridged flow) or between flows with low effusion rates, medium viscosities and small volume (Lastarria SW). Finally, transitions between types with contrasting rheologies (leveed to coulee and leveed to ridged) were not identified.

6. Summary and conclusions

The advance rate of intermediate to silicic lava flows and their morphologies result from the combined effect of topography, effusion rate, and the progressively changing lava flow rheology, governed by

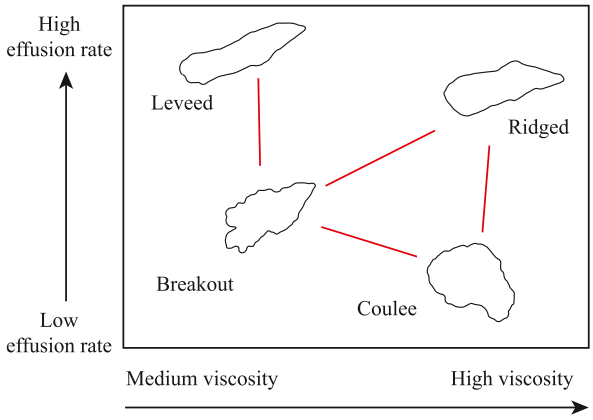

Fig. 16. Qualitative scheme for the division of the identified lava flow types. Red lines represent transitions between the different types. (For interpretation of the references to color in this figure legend, the reader is referred to the web version of this article.)

composition, crystallization, cooling, and crustal growth rates (Farquharson et al., 2015). Moreover, the surface morphology of the lava flows, and especially the shape and wavelength of surface deformations, have been largely discussed as the result of rigid behavior forming faulted ogives or a complex folding process. The generally large value of the dominant wavelength of the surface deformations, comparable in many cases to the mean thickness of the lava flow, suggests that deformation involves a large portion of the lava flow and is possibly controlled by the width of the lava itself.

of the plain-view shape, thickness, surface texture and pre-eruptive topography contribute to better define the field of existence of the different lava types. The FD analysis of the plain-view shape of the flows and the S-transform method based on grayscale images to describe surface textures are two powerful tools to remotely characterize these lava flows, even without availability of high-resolution DEMs. In general, thickness and the maximum dominant wavelength of the folding pattern are not homogeneous along the surface of the flow, with the maximum wavelength spatially related to the local thickness and the flow type. In addition, the maximum dominant wavelength is poorly correlated with SiO_2 content and partially with lava viscosity. Therefore, the control of pre-eruptive topography and viscosity (with variations of several orders of magnitude) on thickness and effusion rate may govern the general dynamics of the flow, directly impacting the different morphological features. This is supported by the positive relationship between the surface maximum wavelength and the gravitational component of the shear stress applied to the lava flow (Fig. 13b).

Mainly based on morphology analysis from remote data, four different types of andesitic to silicic lava flows are distinguished (Fig. 17), together with an additional transitional group:

a) Ridged lavas have highly arcuate ridges with convex surfaces, large thicknesses, long maximum wavelengths, and one rounded frontal lobe. They are high-volume and crystal-rich, and are emplaced under high effusion rates on variably sloping underlying surfaces. The wavelength of deformation, comparable to the thickness, suggests a folding process involving nearly the entire lava flow. They are possibly associated with short-lasting eruptions.
b) Coulee lavas have characteristics between high-viscosity lava flows and domes. They have relatively simple shapes with lengths that do not significantly exceed their widths. Their vents are inside the flow, and large ridges and crumble breccias span the surface. They are emplaced on gentle to medium slopes, with initial radial growth due to inflation of the solidified crust (Griffiths and Fink, 1997). The generally large thickness and the maximum deformation

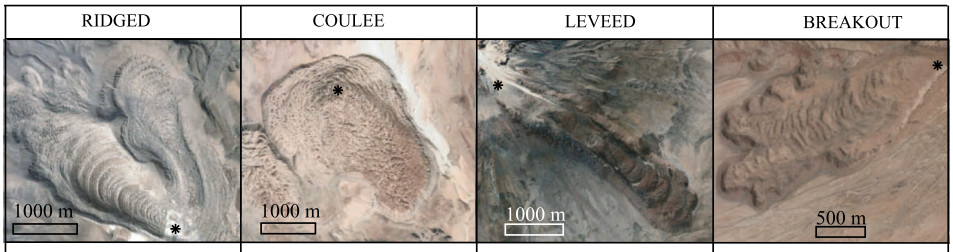

	RIDGED	COULEE	LEVEED	BREAKOUT
Maximum thickness (m)	132 - 274, x = 219	85 - 180, x = 128	70 - 164, x = 115	38 - 182, x = 98
Slope (°)	11 - 32, x = 22	10 - 20, x = 17	~14 in distal areas > 30 in proximal areas	9 - 24, x = 15
Vol (km^3)	0.13- 9.3, x = 2.17	0.11 - 0.55, x = 0.22	0.01 - 0.27, x = 0.11	0.03 - 0.27, x = 0.13
Maximum wavelenght (m)	90 - 274, x = 195	93 - 120, x = 103	58 - 215, x = 103	74 - 285, x = 125
$P_{K\ (>95)}$	3 - 7, x =5.0	2 - 7, x = 4.4	2 - 7, x = 4.1	8 - 14, x = 12.4
Viscosity (Log*n* Pa s)	up to 11.1	up to 9.8	6.2 - 7.0	5.7 - 8.0
Yield strenght (Pa x 10^5)	5.9 - 9.9, x = 7.4	1.6 - 6.5, x = 4.2	1.1 - 9.8, x = 4.5	0.8 - 4.7, x = 2.2
Effusion rate (m^3s^{-1})	130 - 204, x = 164	0.5 - 29, x = 12	3 - 328, x = 89	0.25 - 35, x = 6
Main characteristics	- Arcuate ridges - High volume - Convex surface	- Internal vent - Crumble breccias - Subrounded morphology	- Levees - Unique thick toe - Rough surface - Short to long flows	- Breakout and overflow - Wide fronts - Braided ridges - Thin to thick flows

Fig. 17. Schematic summary of the main types of lava flows identified in the CVZ. x = average values, * = vent location.

wavelength, only a few times the mean thickness and far smaller than the mean lava width, suggest that deformation was mainly dependent on thickness, without an important role of the lateral dimensions of the flow. This implies that only the internal resistance to the flow (viscosity, yield strength), and possibly the effusion rate, controlled deformation. Effusion may prolong for months to years

c) Leveed lavas have the simplest shapes and are highly channelized with a unique frontal toe, generally of maximum thickness. Their channeled nature and steep initial slopes indicate high effusion and advance rates (Gregg and Fink, 2000), while the high velocity of the flow and the gradient between proximal and distal zones induce high stress to the flow, resulting in the formation of distinct surface ridges and throughs with largely variable wavelength spacing, up to several times larger than the mean lava flow thickness.

d) Breakout lavas range from thin to thick flows and have the most complex shapes (high P_k values)with lateral and frontal breakouts, poorly developed levees and fronts with increasing width and thickness. Thin lavas are cooling-limited with relatively low viscosities, with lobes and overflows occurring along the flow margins and at the flow front in areas of low slopes. On the other hand, thicker flows have higher crystal contents and viscosities, while breakouts are less developed and only occur as simple structures, mainly in thermally preferential pathways such as the flow margins.

e) Transitional lavas are common between the different types and exhibit intermediate features, folding patterns, and shapes between the different types, making difficult the univocal attribution to a given lava type.

The strength of the proposed morphology-based characterization, mainly based on data derived from remote observations, is its ready applicability to the analysis of terrestrial and extra-terrestrial lava flows. The analysis also provides key parameters for understanding the main processes that control effusion and emplacement dynamics of intermediate to silicic, crystal-rich lavas, complementing existing lava flow classification, mainly based on the surface morphology characteristics of basaltic lavas.

CRediT authorship contribution statement

Jose Pablo Sepulveda: Conceptualization, Investigation, Writing – original draft, Writing – review & editing, Visualization. **Raffaello Cioni:** Conceptualization, Supervision, Writing – review & editing, Visualization. **Alvaro Aravena:** Conceptualization, Methodology, Software, Writing – review & editing, Visualization.

Declaration of Competing Interest

The authors declare that they have no known competing financial interests or personal relationships that could have appeared to influence the work reported in this paper.

Data availability

Data will be made available on request.

Acknowledgments

This work was supported by the supported by the Agencia Nacional de Investigación y Desarrollo (ANID) - Becas Chile [72200406, 2019]. The TanDEM-X DEMs were provided by the German Aerospace Center (DLR) through proposals DEM_GEOL1342 and DEM_GEOL2956. Alvaro Aravena was financed by the French government IDEX-ISITE initiative 16-IDEX-0001 (CAP 20-25). We thank the editorial assistance of G. Foulger and the constructive comments made by three anonymous

reviewers.

Appendix A. Supplementary data

Supplementary data to this article can be found online at https://doi.org/10.1016/j.earscirev.2023.104433.

References

Anderson, S.W., Fink, J.H., 1992. Crease structures: Indicators of emplacement rates and surface stress regimes of lava flows. Geol. Soc. Am. Bull. 104, 615–625.

Andrews, G.D.M., Kenderes, S.M., Whittington, A.G., Isoma, S.L., Brown, S.R., Pettus, H. D., Cole, B.G., Gokey, K.J., 2020. The fold illusion: the origins and implications of ogives on silicic lavas. Earth Planet. Sci. Lett. 553, 116643 https://doi.org/10.1016/j.epsl.2020.116643.

Bertin, D., Amigo, A., 2019. Geología del volcán San Pedro, Región de Antofagasta. Servicio Nacional de Geología y Minería, Carta Geológica de Chile, Serie Geología Básica. escale 1-50, 000.

Bertin, D., Lara, L., Basualto, D., Amigo, A., Cardona, C., Franco, L., Gil, F., Lazo, J., 2015. High effusion rates of the Cordón Caulle 2011–2012 eruption (Southern Andes) and their relation with the quasi-harmonic tremor. Geophys. Res. Lett. 42, 7054–7063. https://doi.org/10.1002/2015GL064624.

Biot, M.A., 1961. Theory of folding of stratified viscoelastic media and its implications in tectonics and orogenesis. Geol. Soc. Am. Bull. 72 (11), 1595–1620.

Blake, S., 1990. Viscoplastic models of lava domes. In: Fink, J.H. (Ed.), Lava Flows and Domes: Emplacement Mechanisms and Hazard Implications. IAVCEI Proc. in Volcanology, vol. 2. Springer, New York, pp. 88–128.

Borgia, A., Linneman, S.R., Spencer, D., Morales, L.D., Brenes, J.A., 1983. Dynamics of lava flow fronts, Arenal Volcano, Costa Rica. J. Volcanol. Geotherm. Res. 19, 303–329.

Borgia, A., Linneman, S.R., 1990. On the mechanisms of lava flow emplacement and volcano growth: Arenal, Costa Rica. In: Fink, J.H. (Ed.), Lava Flows and Domes: Emplacement Mechanisms and Hazard Implications. IAVCEI Proc. In Volcanology, vol. 2. Springer, New York, pp. 208–243.

Bottinga, Y., Weill, D., 1972. The viscosity of magmatic silicate liquids: a model for calculation. Am. J. Sci. 272, 438–475.

Bullock, L.A., Gertisser, R., O'Driscoll, B., 2018. Emplacement of the Rocche Rosse rhyolite lava flow (Lipari, Aeolian Islands). Bull. Volcanol. 80 (48) https://doi.org/10.1007/s00445-018-1222-4.

Calvari, S., Pinkerton, H., 1998. Formation of lava tubes and extensive flow field during the 1991–93 eruption of Mount Etna. J. Geophys. Res. 103, 27291–27302.

Caricchi, L., Burlini, L., Ulmer, P., Gerya, T., Vassalli, M., Papale, P., 2007. Non-Newtonian rheology of crystal-bearing magmas and implications for magma ascent dynamics. Earth Planet. Sci. Lett. 264 (3–4), 402–419. https://doi.org/10.1016/j.epsl.2007.09.032.

Cas, R.A.F., Wright, J.V., 1988. Volcanic successions modern and ancient: A geological approach to processes, products and successions. Springer Science & Business Media. https://doi.org/10.1007/978-0-412-44640-5.

Cascante, M., 2015. Evolución geológica Y magmática del volcán Isluga, 19° S. Región de Tarapacá, Chile. Universidad de Chile, Santiago, Chile. Master's Thesis.

Cashman, K., Blundy, J., 2000. Degassing and crystallization of ascending andesite and dacite. Philos. Trans. R. Soc. 358, 1487–1513.

Cashman, K., Soule, S., Mackey, B., Deligne, N., Deardorff, N., Dietterich, H., 2013. How lava flows: new insights from applications of lidar technologies to lava flow studies. Geosphere 9 (6), 1664–1680.

Castro, J., Cashman, K.V., 1999. Constraints on rheology of obsidian lavas based on mesoscopic folds. J. Struct. Geol. 21 (7), 807–819.

Castro, J., Cashman, K., Joslin, N., Olmsted, B., 2002. Structural origin of large gas cavities in the Big Obsidian Flow, Newberry Volcano. J. Volcanol. Geotherm. Res. 114 (3–4), 313–330. https://doi.org/10.1016/S0377-0273(01)00296-7.

Castro, J.M., Schipper, C.I., Mueller, S.P., Militzer, A.S., Amigo, A., Silva Parejas, C., Jacob, D., 2013. Storage and eruption of near-liquidus rhyolite magma at Cordón Caulle. Chile. Bull. Volcanol. 75, 702. https://doi.org/10.1007/s00445-013-0702-9.

Castruccio, A., Rust, A.C., Sparks, R.S.J., 2010. Rheology and flow of crystal-bearing lavas: Insights from analogue gravity currents. Earth Planet. Sci. Lett. 297, 471–480. https://doi.org/10.1016/j.epsl.2010.06.051.

Castruccio, A., Rust, A.C., Sparks, R.S.J., 2013. Evolution of crust- and core-dominated lava flows using scaling analysis. Bull. Volcanol. 75 (68) https://doi.org/10.1007/s00445-012-0681-2.

Chevrel, M.O., Platz, T., Hauber, E., Baratoux, D., Lavallée, Y., Dingwell, D.B., 2013. Lava flow rheology: a comparison of morphological and petrological methods. Earth Planet. Sci. Lett. 384, 102–120.

Cioni, R., Funedda, A., 2005. Structural geology of crystal-rich, silicic flows: a case study from San Pietro Island (Sardinia, Italy). Geol. Soc. Am. 396, 1–14. https://doi.org/10.1130/2005.2396(01).

Cimarelli, C., Costa, A., Mueller, S.P., Mader, H.M., 2011. Rheology of magmas with bimodal crystal size and shape distributions: Insights from analog experiments. Geochem. Geophys. Geosyst. 12, Q07024. https://doi.org/10.1029/2011GC003606.

Costa, A., 2005. Viscosity of high crystal content melts: Dependence on solid fraction. Geophys. Res. Lett. 32, L22308. https://doi.org/10.1029/2005gl024303.

Costa, A., Caricchi, L., Bagdassarov, N., 2009. A model for the rheology of particle-bearing suspensions and partially molten rocks. Geochem. Geophys. Geosyst. 10, Q03010. https://doi.org/10.1029/2008gc002138.

Deardorff, N.D., Cashman, K.V., 2012. Emplacement conditions of the c. 1,600-year bp Collier Cone lava flow, Oregon: a LiDAR investigation. Bull. Volcanol. 74 (9), 2051–2066. https://doi.org/10.1007/s00445-012-0650-9.

Deardorff, N., Booth, A., Cashman, K., 2019. Remote characterization of dominant wavelengths from surface folding on lava flows using lidar and discrete Fourier transform analyses. Geochem. Geophys. Geosyst. 20, 3952–3970. https://doi.org/10.1029/2019GC008497.

De Reu, J., Bourgeois, J., Bats, M., Zwertvaegher, A., Gelorini, V., De Smedt, P., Chu, W., Antrop, M., De Maeyer, P., Finke, P., Van Meirvenne, M., Verniers, J., Crombé, P., 2013. Application of the topographic position index to heterogeneous landscapes. Geomorphology 186, 39–49. https://doi.org/10.1016/j.geomorph.2012.12.015.

De Silva, S.L., Self, S., Francis, P.W., Drake, R.E., Ramirez, C., 1994. Effusive silicic volcanism in the Central Andes: the Chao dacite and other young lavas of the Altiplano-Puna Volcanic complex. J. Geophys. Res. 99 (B9), 17805–17820.

De Silva, S.L., Davidson, J.P., Croudace, I.W., Escobar, A., 1993. Volcanological and petrological evolution of Volcan Tata Sabaya, SW Bolivia. J. Volcanol. Geotherm. Res. 55, 305–335.

Dictionary, Merrian-Webster, 2002. https://www.merriam-webster.com/dictionary/classification accesed 28 Marrch, 2023.

Dietterich, H.R., Poland, M.P., Schmidt, D.A., Cashman, K.V., Sherrod, D.R., Espinosa, A. T., 2012. Tracking lava flow emplacement on the east rift zone of Kilauea, Hawaii, with synthetic aperture radar coherence. Geochem. Geophys. Geosyst. 13, Q05001 https://doi.org/10.1029/2011GC004016.

Dietterich, H.R., Cashman, K.V., 2014. Channel networks within lava flows: Formation, evolution, and implications for flow behavior. J. Geophys. Res. Earth Surf. 119, 1704–1724. https://doi.org/10.1002/2014JF003103.

Dietterich, H.R., Cashman, K.V., Rust, C.A., Lev, E., 2015. Diverting lava flows in the lab. Nat. Geosci. 8, 494–496. https://doi.org/10.1038/ngeo2470.

Dinas, S., Bañon, J.M., 2014. A review on Delaunay Triangulation with application on computer vision. Int. J. Comput. Sci. Eng. 3, 2.

Dunai, T.J., González López, G.A., Juez-Larré, J., 2005. Oligocene-Miocene age of aridity in the Atacama Desert revealed by exposure age dating of erosion-sensitive landforms. Geology 33, 321–324.

Farquharson, J.I., James, M.R., Tuffen, H., 2015. Examining rhyolite lava flow dynamics through photo-based 3D reconstructions of the 2011–2012 lava flow field at Cordón-Caulle, Chile. J. Volcanol. Geotherm. Res. 304, 336–348.

Farrell, J., Karson, J., Soldati, A., Wysocki, R., 2018. Multiple-generation folding and non-coaxial strain of lava crusts. Bull. Volcanol. 80 (84) https://doi.org/10.1007/s00445-018-1258-5.

Farris, R.J., 1968. Prediction of the viscosity of multimodal suspensions from unimodal viscosity data. Trans. Soc. Rheol. 12, 281–301.

Favalli, M., Fornaciai, A., Nannipieri, L., Harris, A., Calvari, S., Lormand, C., 2018. Bull. Volcanol. 80 (29) https://doi.org/10.1007/s00445-018-1192-6.

Feeley, T.C., Davidson, J.P., Armendia, A., 1993. The volcanic and magmatic evolution of volcan Ollagüe, a high-K, late Quaternary stratovolcano in the andean Central Volcanic Zone. J. Volcanol. Geotherm. Res. 54, 221–245.

Figueroa, O., Deruelle, B., Demaiffe, D., 2009. Genesis of adakite-like lavas of Licancabur volcano (Chile-Bolivia, Central Andes). C.R. Geoscience 341, 310–318.

Finch, R.H., 1933. Block lavas. J. Geol. 41, 769–770.

Fink, J.H., 1980. Surface folding and viscosity of rhyolite flows. Geology 8 (5), 250–254.

Fink, J.H., 1983. Structure and emplacement of a rhyolitic obsidian flow: little glass mountain, medicine lake highland, northern California. Geol. Soc. Am. Bull. 94, 362–380.

Fink, J.H., Fletcher, R.C., 1978. Ropy pahoehoe: Surface folding of a viscous fluid. J. Volcanol. Geotherm. Res. 4 (1–2), 151–170.

Fink, J.H., Griffiths, R.W., 1990. Radial spreading of viscous-gravity currents with solidifying crust. J. Fluid Mech. 2 (21), 485–510.

Fink, J.H., Griffiths, R.W., 1998. Morphology, eruption rates, and rheology of lava domes: insights from laboratory models. J. Geophys. Res. 103, 527–545.

Gardeweg, M., Cornejo, P., Davidson, J., 1984. Geología del volcan Llullaillaco, altiplano de Antofagasta, Chile (Andes Centrales). Rev. Geol. Chile 23, 21–37.

Gardeweg, M., Amigo, A., Mattews, S.J., Sparks, R.S.J., Clavero, J., 2011. Geología del volcan Lascar region de Antofagasta. Servicio Nacional de Geología y Minería, Carta Geologica de Chile. Ser. Geol. Basica 131. Escale 1:50,000.

Giordano, D., Russell, J.K., Dingwell, D.B., 2008. Viscosity of magmatic liquids: a model. Earth Planet. Sci. Lett. 271 (1–4), 123–134. https://doi.org/10.1016/j.epsl.2008.03.038.

Giordano, D., 2019. Advances in the rheology of natural multiphase silicate melts: importance for magma transport and lava flow emplacement. Ann. Geophys. 62 (2) https://doi.org/10.4401/ag-7859. VO216.

Glasbey, C.A., Horgan, C.W., 1995. In: Image Analysis for the Biological Sciences, 605. John Wiley & Sons Inc, New York, p. 218 pp..

Glaze, L., Baloga, S.M., Garry, W.B., Fagents, S.A., Parcheta, C., 2009. A hybrid model for leveed lava flows: Implications for eruption styles on Mars. J. Geophys. Res. 114, E07001. https://doi.org/10.1029/2008JE0032.

Gregg, T.K.P., Fink, J.H., 1995. Quantification of submarine lava-flow morphology through analog experiments. Geology 23, 73–76.

Gregg, T.K.P., Fink, J.H., 1996. Quantification of extraterrestrial lava flow effusion rates through laboratory simulations. J. Geophys. Res. 101, 16891–16900.

Gregg, T.K., Fink, J.H., Griffiths, R.W., 1998. Formation of multiple fold generations on lava flow surfaces: Influence of strain rate, cooling rate, and lava composition. J. Volcanol. Geotherm. Res. 80 (3–4), 281–292. https://doi.org/10.1016/S0377-0273(97)00048-6.

Gregg, T.K.P., Fink, J.H., 2000. A laboratory investigation into the effects of slope on lava flow morphology. J. Volcanol. Geotherm. Res. 96, 145–159. https://doi.org/10.1016/S0377−0273(99)00148−1.

Griffiths, R.W., Fink, J.H., 1992a. Solidification and morphology of submarine lavas: a dependence on extrusion rate. J. Geophys. Res. 97, 19729–19737.
Griffiths, R.W., Fink, J.H., 1992b. The morphology of lava flows in planetary environments: predictions from analog experiments. J. Geophys. Res. 97, 19739–19748.
Griffiths, R.W., Fink, J.H., 1997. Solidifying Bingham extrusions: a model for the growth of silicic lava domes. J. Fluid Mech. 347, 13–36.
Griffiths, R., 2000. The dynamics of lava flows. Annu. Rev. Fluid Mech. 32 (1), 477–518. https://doi.org/10.1146/annurev.fluid.32.1.477.
Griffiths, R.W., Kerr, R.C., Cashman, K.V., 2003. Patterns of solidification in channel flows with surface cooling. J. Fluid Mech. 496, 33–62.
Grosse, P., Orihashi, Y., Guzman, S., Sumino, H., Nagao, K., 2018. Eruptive history of Incahuasi, Falso Azufre and El Cóndor Quaternary composite volcanoes, southern Central Andes. Bull. Volcanol. 80 (44) https://doi.org/10.1007/s00445-018-1221-5.
Gualda, G.A.R., Ghiorso, M.S., Lemons, R.V., Carley, T.L., 2012. Rhyolite-MELTS: a modified calibration of MELTS optimized for silica-rich, fluid-bearing magmatic systems. J. Petrol. 53, 875–890.
Hallworth, M.A., Huppert, H.E., Sparks, R.S.J., 1987. A laboratory simulation of basaltic lava flows. Mod. Geol. 11, 93–107.
Harris, A.J.L., Flynn, L.P., Matias, O., Rose, W.I., 2002. The thermal stealth flows of Santiaguito dome, Guatemala: Implications for the cooling and emplacement of dacitic block-lava flows. Geol. Soc. Am. Bull. 114 (5), 533–546. https://doi.org/10.1130/0016-7606(2002)114<0533:TTSFOS>2.0.CO;2.
Harris, A.J.L., Dehn, J., Calvari, S., 2007. Lava effusion rate definition and measurement: a review. Bull. Volcanol. 70, 1–22. https://doi.org/10.1007/s00445-007-0120-y.
Harris, A.J.L., Rowland, S.K., 2009. Effusion rate controls on lava flow length and the role of heat loss: A review. In: Thordarson, T., Self, S., Larsen, G., Rowland, S.K., Hoskuldsson, A. (Eds.), Studies in Volcanology: The Legacy of George Walker, 2, pp. 33–51. Special Publications of IAVCEI.
Harris, A.J.L., Rowland, S.K., 2015. Lava flows and rheology. In: Sigurdsson, H., Houghton, B., McNutt, S.R., Rymer, H., Styx, J. (Eds.), Encyclopedia of Volcanoes, 2nd Edition. Academic Press, pp. 321–342. https://doi.org/10.1016/C2015-0-00175-7.
Harris, A.J.L., Rowland, S., Villenueve, N., Thordarson, T., 2016. Pāhoehoe, ʻaʻā, and block lava: an illustrated history of the nomenclature. Bull. Volcanol. 79 (7) https://doi.org/10.1007/s00445-016-1075-7.
Heckbert, P., 1982. Color image quantization for frame buffer display. Comput. Graph. 16 (3), 297–307.
Hulme, G., 1974. The interpretation of lava flow morphology. Geophys. 39 (2), 361–383. https://doi.org/10.1111/j.1365-246X.1974.tb05460.x.
Hunt, J.A., Pyle, D.M., Mather, T.A., 2019. The geomorphology, structure, and lava flow dynamics of peralkaline rift volcanoes from high-resolution digital elevation models. Geochem. Geophys. Geosyst. 20, 1508–1538. https://doi.org/10.1029/2018GC008085.
Jeffreys, H., 1925. The flow of water in an inclined channel of rectangular section. Philos. Mag. Ser. 6,49 (293), 793–807.
Jones, A.E., 1943. Classification of lava surfaces. Am. Geophys. Union Trans. 1, 265–268.
Kereszturi, G., Németh, K., Moufti, M.R., Cappello, A., Murcia, H., Ganci, G., Del Negro, C., Procter, J., Zahran, H.M.A., 2016. Emplacement conditions of the 1256AD Al-Madinah lava flow field in Harrat Rahat, Kingdom of Saudi Arabia-Insights from surface morphology and lava flow simulations. J. Volcanol. Geotherm. Res. 309, 14–30.
Kerr, C.R., Griffiths, R.W., Cashman, K., 2006. Formation of channelized lava flows on an unconfined slope. J. Geophys. Res. 111 (B10), B10,206. https://doi.org/10.1029/2005JB004225.
Kilburn, C., 1990. Surfaces of aa flow-fields on Mount-Etna, Sicily: morphology, rheology, crystallization and scaling phenomena. In: Fink, J.H. (Ed.), Lava Flows and Domes, IAVCEI Proceedings in Volcanology, vol. 2. Springer, New York, pp. 129–156.
Kilburn, C.R.J., 2000. Lava flows and flow fields. In: Sigurdsson, H. (Ed.), Encyclopedia of Volcanoes. Academic Press, San Diego, pp. 291–305.
Kilburn, R.C., 2004. Fracturing as a quantitative indicator of lava flow dynamics. J. Volcanol. Geotherm. Res. 132 (2–3), 209–224.
Klein, J., Mueller, S.P., Castro, J.M., 2017. The influence of crystal size distributions on the rheology of magmas: New insights from analog experiments. Geochem. Geophys. Geosyst. 18, 4055–4073. https://doi.org/10.1002/2017GC007114.
Klein, J., Mueller, S.P., Helo, C., Schweitzer, S., Gurioli, L., Castro, J.M., 2018. An expanded model and application of the combined effect of crystal-size distribution and crystal shape on the relative viscosity of magmas. J. Volcanol. Geotherm. Res. S0377–0273 (17) https://doi.org/10.1016/j.jvolgeores.2018.04.018, 30725-4.
Krieger, G., Moreira, A., Fiedler, H., Hajnsek, I., Werner, M., Younis, M., Zink, M., 2007. TanDEM-X: a satellite formation for high-resolution SAR interferometry. IEEE Trans. Geosci. Remote Sens. 45 (11), 3317–3341.
Krieger, I.M., Dougherty, T.J., 1959. A mechanism for non-Newtonian flow in suspensions of rigid spheres. J. Rheol. 3, 137.
Latutrie, B., Harris, A., Médard, E., Gurioli, L., 2017. Eruption and emplacement dynamics of a thick trachytic lava flow of the Sancy Volcano (France). Bull. Volcanol. 79 (4) https://doi.org/10.1007/s00445-016-1084-6.
Leggett, T.N., Befus, K.S., Kenderes, S.M., 2020. Rhyolite lava emplacement dynamics inferred from surface morphology. J. Volcanol. Geotherm. Res. 395, 106850 https://doi.org/10.1016/j.jvolgeores.2020.106850.
Lescinsky, D.T., Skoblenick, S.V., Mansinha, L., 2007. Automated identification of lava flow structures using local Fourier spectrum of digital elevation data. J. Geophys. Res. 112 (B05212) https://doi.org/10.1029/2006 JB004263.
Lev, E., Rumpf, E., Dietterich, H., 2019. Analog experiments of lava flow emplacement. Ann. Geophys. 62, 2 (vo225) https://doi.org/10.4401/ag-7843.
Lister, J.R., 1992. Viscous flows down an inclined plane from point and line sources. J. Fluid Mech. 242, 631–653.
Lyman, A.W., Koenig, E., Fink, J., 2004. Predicting yield strengths and effusion rates of lava domes from morphology and underlying topography. J. Volcanol. Geotherm. Res. 129, 125–138. https://doi.org/10.1016/S0377-0273(03)00236-1.
Macdonald, G.A., 1953. Pahoehoe, aa and block lava. Am. J. Sci. 251, 169–191.
Macdonald, G.A., 1967. Forms and structures of extrusive basaltic rocks. In: Hess, H.H., Poldervaart, A. (Eds.), The Poldervaart Treatise on rocks of basaltic composition. Interscience, New York, pp. 1–61.
Macdonald, G.A., 1972. Volcanoes. In: Prentice Hall Inc., Englewood Cliffs, p. 501.
Magnall, N., James, M.R., Tuffen, H., Vye-Brown, C., 2017. Emplacing a Cooling-Limited Rhyolite Lava Flow: Similarities with Basaltic Lava Flows. Front. Earth Sci. 5 (44) https://doi.org/10.3389/feart.2017.00044.
Magnall, N., James, M.R., Tuffen, H., Vye-Brown, C., Schipper, C.I., Castro, J., Gerard Davies, A., 2018. The origin and evolution of breakouts in a cooling-limited rhyolite lava flow. Geol. Soc. Am. Bull. 131 (1/2), 137–154.
Mamani, M., Wörner, G., Sempere, T., 2010. Geochemical variations in igneous rocks of the Central andean orocline (13°S to 18°S): Tracing crustal thickening and magma generation through time and space. Geol. Soc. Am. Bull. 122 (1/2), 162–182. https://doi.org/10.1130/B26538.1.
Manley, C.R., Fink, J.H., 1987. Internal textures of rhyolite flows as revealed by research drilling. Geology 15, 549–552. https://doi.org/10.1130/0091-7613(1987)15<549:ITORFA>2.0.CO;2.
Martinez, S., 2019. Evolución magmática y geoquímica de la Cadena volcánica Olca-Paruma (20°57'S-68°30'O), Norte de Chile. Universidad Católica del Norte, Antofagasta, Chile. Undergraduated Thesis.
Moore, H.J., Arthur, D.W.G., Schaber, G.G., 1978. Yield strengths of flows on the Earth, Moon, and Mars. In: Lunar and Planetary Science Conference, 9, pp. 750–751.
Mueller, S.P., Llewellin, E.W., Mader, H.M., 2011. The effect of particle shape on suspension viscosity and implications for magmatic flows. Geophys. Res. Lett. 38, L13316. https://doi.org/10.1029/2011GL047167.
Naranjo, J.A., 1992. Chemistry and petrological evolution of the Lastarria volcanic complex in the north chilean Andes. Geol. Mag. 129 (6), 723–740.
Naranjo, J., Sparks, R., Stasiuk, M., Moreno, H., Ablay, G., 1992. Morphological, structural and textural variations in the 1988–1990 andesite lava of Lonquimay Volcano, Chile. Geol. Mag. 129 (6), 657–678. https://doi.org/10.1017/S0016756800008426.
Naranjo, J.A., 2010. Geología del Complejo Volcánico Lastarria, Región de Antofagasta. Servicio Nacional de Geología y Minería, Carta Geológica de Chile, Serie Geología Básica, Santiago.
Naranjo, J., Villa, V., Venegas, C., 2013. Geología de Las áreas Salar de Pajonales Y Cerro Moño, Regiones de Antofagasta Y Atacama. In: Servicio Nacional de Geología y Minería, Carta Geológica de Chile, Serie Geología Básica, pp. 153–154.
Navarro-Ochoa, C., Gavilanes-Ruiz, J.C., Cortes-Cortes, A., 2002. Movement and emplacement of lava flows at Volcan de Colima, Mexico: November 1998-February 1999. J. Volcanol. Geotherm. Res. 117, 155–167.
Pallister, J.S., Diefenbach, A.K., Burton, W.C., Muñoz, J., Griswold, J.P., Lara, L.E., Lowenstern, J.B., Valenzuela, C.E., 2013. The Chaitén rhyolite lava dome: Eruption sequence, lava dome volumes, rapid effusion rates and source of the rhyolite magma. Andean. Geology 40 (2). https://doi.org/10.5027/andgeoV40n2-a06.
Persoon, E., Fu, K.S., 1977. Shape Discrimination using Fourier Descriptors. IEEE Trans. Syst. Man Cybernet. 7 (3), 170–179.
Pinkerton, H., Sparks, R.S.J., 1976. The 1975 sub-terminal lavas, Mount Etna: a case history of the formation of a compound lava field. J. Volcanol. Geotherm. Res. 1, 167–182.
Pinkerton, H., Stevenson, R.J., 1992. Methods of determining the rheological properties of magmas at sub-liquidus temperatures. J. Volcanol. Geotherm. Res. 53, 47–66.
Pinkerton, H., Wilson, L., 1994. Factors controlling the lengths of channel-fed lava flows. Bull. Volcanol. 56, 108–120.
Pyle, D.M., Elliott, J.R., 2006. Quantitative morphology, recent evolution, and future activity of the Kameni Islands volcano, Santorini. Greece. Geosphere 2 (5), 253–268.
Reyes Hardy, M.P., Aguilera Barraza, F., Sepulveda Birke, J.P., Esquivel Cáceres, A., Inostroza Pizarro, M., 2021. GIS-based volcanic hazards, vulnerability and risks assessment of the Guallatiri Volcano, Arica y Parinacota Region, Chile. J. S. Am. Earth. Sci. 109, 103262.
Richardson, P., Karlstrom, L., 2019. The multi-scale inffluence of topography on lava flow morphology. Bull. Volcanol. 81, 21. https://doi.org/10.1007/s00445-019-1278-9.
Rivera, M., Martin, H., Le Pennec, H.L., Thouret, J.C., Gourgad, A., Gerbe, M.C., 2017. Petro-geochemical constraints on the source and evolution of magmas at El Misti volcano (Peru). Lithos 268–271, 240–259. https://doi.org/10.1016/j.lithos.2016.11.009.
Rodriguez, I., Roche, O., Moune, S., Aguilera, F., Campos, E., Pizarro, M., 2015. Evolution of Irruputuncu volcano, Central Andes, northern Chile. J. S. Am. Earth Sci. 63, 385–399. https://doi.org/10.1016/j.jsames.2015.08.012.
Sato, H., Suzuki-Kamata, K., Sato, E., Sano, K., Wada, K., Imura, R., 2013. Viscosity of andesitic lava and its implications for possible drain-back processes in the 2011 eruption of the Shinmoedake volcano, Japan. Earth Planets Space 65, 623–631.
Schneider, C.A., Rasband, W.S., Eliceiri, K.W., 2012. NIH image to ImageJ: 25 years of image analysis. Nat. Methods 9 (7), 671–675. https://doi.org/10.1038/nmeth.2089.
Selles, D., Gardeweg, M., 2018. Geología del área Ascotán-Cerro Inacaliri, Región de Antofagasta. Servicio Nacional de Geología y Minería, Carta Geológica de Chile. Ser. Geol. Básica 190. Escale 1, 50,000. https://doi.org/10.13140/RG.2.2.30946.84165.
Sepulveda, J.P., Aguilera, F., Inostroza, M., Reyes, M.P., 2021. Geological evolution of the Guallatiri volcano, Arica y Parinacota Region, northern Chile. J. S. Am. Earth Sci. 107 (103117) https://doi.org/10.1016/j.jsames.2020.103117.

Shaw, H.R., 1972. Viscosities of magmatic silicate liquids: an empirical method of prediction. Am. J. Sci. 272, 870–893.
Sparks, R.S.J., Folkes, C.B., Humphreys, M.C.S., Barfod, D.N., Clavero, J., Sunagua, M.C., Mcnutt, S.R., Pritchard, M.E., 2008. Uturuncu volcano, Bolivia: volcanic unrest due to mid-crustal magma intrusion. Am. J. Sci. 308, 727–769. https://doi.org/10.2475/06.2008.01.
Stern, C., 2004. Active andean volcanism: its geologic and tectonic setting. Rev. Geol. Chile 31 (2). https://doi.org/10.4067/S0716-02082004000200001.
Stockwell, R., Mansinha, L., Lowe, R., 1996. Localization of the complex spectrum: the S-transform. IEEE Trans. Signal Process. 44 (4), 998–1001.
Stockwell, R., 2007. A basis for efficient representation of the S-transform. Digit. Signal Process. 17, 371–393. https://doi.org/10.1016/j.dsp.2006.04.006.
Swanson, S.E., Naney, M.T., Westrich, H.R., Eichelberger, J.C., 1989. Crystallization history of Obsidian dome, Inyo domes, California. Bull. Volcanol. 51 (3), 161–176.
Tolometti, G.D., Neish, C.D., Osinski, G.R., Hughes, S.S., Kobs Nawotniak, S.E., 2020. Interpretations of lava flow properties from radar remote sensing data. Planet. Space Sci. 190, 104991 https://doi.org/10.1016/j.pss.2020.104991.
Tuffen, H., James, M.R., Castro, J.M., Schipper, C.I., 2013. Exceptional mobility of an advancing rhyolitic obsidian flow at Cordón Caulle volcano in Chile. Nat. Commun. 4 (1) https://doi.org/10.1038/ncomms3709.
Vallance, J.W., Schneider, D.J., Schilling, S.P., 2008. Growth of the 2004-2006 lava-dome complex at Mount St. Helens, Washington. In: A Volcano Rekindled, pp. 2004–2006.
Wadge, W., Voight, B., Sparks, R.S.J., Cole, P.D., Loughlin, S.C., Robertson, R.E.A., 2014. An overview of the eruption of Soufrie`re Hills Volcano, Montserrat from 2000 to 2010. In: Wadge, G., Robertson, R.E.A., Voight, B. (Eds.), The Eruption of Soufriere Hills Volcano, Montserrat from 2000 to 2010, 39. Geological Society, London, Memoirs. https://doi.org/10.1144/M39.
Walker, G.P.L., 1967. Thickness and Viscosity of Etnean Lavas. Nature 213, 484–485.
Walker, G.P.L., 1973. Factors controlling the lengths of lava flows. Philos. Trans. R. Soc. London 274, A107–A118.
Watts, R.B., Herd, R.A., Sparks, R.S.J., Young, S.R., 2002. Growth patterns and emplacement of the andesitic lava dome at Soufrière Hills Volcano, Montserrat. In: Druitt, T.T., Kokelaar, B.P. (Eds.), The Eruption of Soufrière Hills Volcano, Montserrat, from 1995 to 1999. Geological Society, London, Memoirs, p. 21.
Wentworth, C.K., Macdonald, G.A., 1953. Structures and forms of basaltic rocks in Hawaii. Bulletin 994, USGS int. Report, 98 pp.
Wörner, G., Lopez-Escobar, L., Moorbath, S., Horn, S., Entenmann, J., Harmon, R.S., Davidson, J.P., 1992. Variaciones geoquímicas, locales y regionales, en el frente volcanico cuaternario de los andes centrales (17° 30′ -22° 00′ S). Norte Chile. Rev. Geol. Chile 19, 37–55.
Wörner, G., Schildgen, T.F., Reich, M., 2018. The Central Andes: elements of an Extreme Land. Elements 14, 225-23.